

# The $T_e[\text{N II}]-T_e[\text{O III}]$ temperature relation in H II regions and the reliability of strong-line methods

K. Z. Arellano-Córdova<sup>1,2\*</sup> and M. Rodríguez<sup>1</sup>

<sup>1</sup>*Instituto Nacional de Astrofísica, Óptica y Electrónica (INAOE), Apdo. Postal 51 y 216, Puebla, Mexico*

<sup>2</sup>*Instituto de Astrofísica de Canarias, E-38200 La Laguna, Tenerife, Spain*

Accepted XXX. Received YYY; in original form ZZZ

## ABSTRACT

We use a sample of 154 observations of 124 H II regions that have measurements of both  $T_e[\text{O III}]$  and  $T_e[\text{N II}]$ , compiled from the literature, to explore the behaviour of the  $T_e[\text{O III}]-T_e[\text{N II}]$  temperature relation. We confirm that the relation depends on the degree of ionization and present a new set of relations for two different ranges of this parameter. We study the effects introduced by our temperature relations and four other available relations in the calculation of oxygen and nitrogen abundances. We find that our relations improve slightly on the results obtained with the previous ones. We also use a sample of 26 deep, high-resolution spectra to estimate the contribution of blending to the intensity of the temperature-sensitive line  $[\text{O III}] \lambda 4363$ , and we derive a relation to correct  $T_e[\text{O III}]$  for this effect. With our sample of 154 spectra, we analyse the reliability of the R, S, O3N2, N2, ONS, and C strong-line methods by comparing the metallicity obtained with these methods with the one implied by the direct method. We find that the strong-line methods introduce differences that reach  $\sim 0.2$  dex or more, and that these differences depend on O/H, N/O, and the degree of ionization.

**Key words:** ISM: abundances – H II regions – galaxies: abundances.

## 1 INTRODUCTION

H II regions provide fundamental information about the chemical composition of the present-day interstellar medium, which is crucial to understand the chemical evolution of galaxies. The electron temperature is one of the two main physical conditions that characterize the ionized gas, and this parameter plays a very important role in abundance determinations. The measurement of the electron temperature is based on the detection of weak emission lines, like  $[\text{O III}] \lambda 4363$ ,  $[\text{N II}] \lambda 5755$ ,  $[\text{S II}] \lambda 6312$ , and  $[\text{O II}] \lambda \lambda 7320, 7330$ . Deep spectra that cover a wide spectral range allow the measurement of more than one electron temperature, each one of them associated to a particular ion. This provides the opportunity to characterize each zone of the nebula by a different temperature (e.g. Peimbert 2003; Kennicutt et al. 2003; Esteban et al. 2004, 2015; Berg et al. 2015; Toribio San Cipriano et al. 2016; Croxall et al. 2016).

A common approach is to associate the ions with low degree of ionization, such as  $\text{O}^+$ ,  $\text{N}^+$ , and  $\text{S}^+$ , to  $T_e[\text{O II}]$  or  $T_e[\text{N II}]$ , and the ions with high degree of ionization, such as  $\text{O}^{++}$ ,  $\text{S}^{++}$ , and  $\text{Ne}^{++}$ , to  $T_e[\text{O III}]$ .  $T_e[\text{N II}]$  and  $T_e[\text{O III}]$  are the

temperatures more commonly used to represent the nebular structure, because there are several problems involved in the determination of  $T_e[\text{O II}]$  and  $T_e[\text{S III}]$ . Some problems related to  $T_e[\text{O II}]$  are its dependence on the electron density, the contribution from recombination to the emission of  $[\text{O II}] \lambda \lambda 7320, 7330$ , which is difficult to estimate, and the fact that the  $[\text{O II}] \lambda \lambda 7320, 7330$  lines are located in a zone of the spectrum which is contaminated by telluric lines. Besides, the  $[\text{O II}] \lambda 3727/\lambda \lambda 7320, 7330$  ratio is more sensitive to the reddening correction than other diagnostics. In the case of  $T_e[\text{S III}]$ , the  $[\text{S III}] \lambda \lambda 9069, 9532$  emission lines are in a wavelength range where strong telluric emission and absorptions lines are present (Stevenson 1994). The correction for these effects is a difficult task and the uncertainties related to this correction are very hard to quantify.

In extragalactic H II regions with spectra of medium quality it is common to measure only one electron temperature, usually  $T_e[\text{O III}]$  or  $T_e[\text{N II}]$ . However, due to the temperature gradients observed in ionized nebulae, having different measurements to characterize the nebular temperature structure will result in better estimates of the chemical abundances. Several studies have provided different temperature relations that can be used to estimate  $T_e[\text{N II}]$  or  $T_e[\text{O III}]$  when only one of these temperatures is measured.

\* E-mail: karlaz@inaoep.mx (A-CKZ)

These temperature relations are either based on photoionization models (Campbell et al. 1986; Garnett 1992; Pagel et al. 1992; Izotov et al. 1997; Deharveng et al. 2000; Pérez-Montero & Contini 2009; Pérez-Montero 2014) or observational data (Pilyugin et al. 2006; Pilyugin 2007; Esteban et al. 2009; Berg et al. 2015; Croxall et al. 2016; Yates et al. 2019).

On the other hand, strong-line methods provide an opportunity to derive chemical abundances, mainly the oxygen abundance, usually taken as a proxy for metallicity in H II regions, when the electron temperature is not measured. These methods are calibrated using either observational data, photoionization models or a combination of both (e.g. McGaugh 1991; Denicoló et al. 2002; Kobulnicky & Kewley 2004; Pilyugin & Thuan 2005; Kewley & Ellison 2008). Stasińska (2010) showed that the abundances derived with strong-line methods may be significantly biased if the objects studied do not share the same properties (for instance, the hardness of the ionizing radiation) as the objects used in the calibration sample. Therefore, the performance of strong-line methods depends on the characteristics of their calibration sample, and strong-line methods based on observational data must use large samples of H II regions. In most cases, only one estimate of the electron temperature will be available for each region, making it necessary to use temperature relations (Pilyugin et al. 2010b, 2012a; Marino et al. 2013). Improvements in the derived temperature relations will help to provide better estimates of chemical abundances also in this case.

In this paper, we present an analysis of the  $T_e[\text{N II}]$ - $T_e[\text{O III}]$  temperature relation based on a large sample of optical spectra of H II regions from different galaxies compiled from the literature. We also study the behaviour of some strong-line methods by comparing their results with those obtained with the direct method.

## 2 SAMPLE

Our initial sample contains 168 spectra of 133 H II regions compiled from the literature. The spectral resolutions are in the range 0.1-10 Å, but most observations have spectral resolutions larger than 5 Å. The 168 observed spectra have measurements of both  $[\text{O III}] \lambda 4363$  and  $[\text{N II}] \lambda 5755$ , which makes it possible to compute the electron temperatures  $T_e[\text{N II}]$  and  $T_e[\text{O III}]$ . The line intensities were taken from Esteban et al. (2002); Luridiana et al. (2002); Kennicutt et al. (2003); Nazé et al. (2003); Peimbert (2003); Tsamis et al. (2003); Esteban et al. (2004); García-Rojas et al. (2004); Izotov & Thuan (2004); García-Rojas et al. (2005); Hägele et al. (2006); García-Rojas et al. (2006, 2007); Bresolin (2007); Copetti et al. (2007); López-Sánchez et al. (2007); Hägele et al. (2008); Bresolin et al. (2009); Esteban et al. (2009); Mesa-Delgado et al. (2009); Stanghellini et al. (2010); Guseva et al. (2011); Patterson et al. (2012); Peña-Guerrero et al. (2012); Zurita & Bresolin (2012); Berg et al. (2013); Esteban et al. (2014); Miralles-Caballero et al. (2014); Berg et al. (2015); Esteban et al. (2016); Croxall et al. (2016); Toribio San Cipriano et al. (2016); Esteban et al. (2017); Espiritu et al. (2017); Fernández-Martín et al. (2017); Toribio San Cipriano et al. (2017).

The initial sample was filtered following the criteria de-

finied below in Section 4.1. The final sample contains 154 spectra of 124 H II regions. Table A1 in Appendix A, whose full version is available online, lists the sample H II regions and the references for their spectra (column 10), along with the galaxy to which they belong and the identifications used in the original references (columns 2 and 3). Table A1 also provides the identification number that we use for each object (column 1) and the values we derive for the electron density and temperature (columns 4 to 7), the oxygen abundance, and the nitrogen to oxygen abundance ratio (columns 8 and 9). The values of the physical conditions and chemical abundances were derived following the procedure described below.

## 3 PHYSICAL CONDITIONS AND CHEMICAL ABUNDANCES

We carry out a homogeneous analysis using the line fluxes corrected for extinction compiled from the literature. We use the Python package PYNEB (Luridiana, Morisset & Shaw 2015) to determine physical conditions and chemical abundances. Table 1 shows the atomic data sets from PYNEB that we use in our calculations. Since we are avoiding the problematic data sets identified by Juan de Dios & Rodríguez (2017), and since the sample objects have relatively small electron densities, a change in atomic data would lead to absolute variations lower than 7 per cent in temperature and lower than 0.15 dex in the abundance ratios derived here (Juan de Dios & Rodríguez 2017).

### 3.1 Electron temperature and density

The electron density was calculated using the line intensity ratios  $[\text{S II}] \lambda 6717/\lambda 6731$  and, for several objects,  $[\text{O II}] \lambda 3729/\lambda 3726$ . In objects where it was possible to use both density diagnostics we use the mean value of the density. We obtain very low densities ( $n_e < 100 \text{ cm}^{-3}$ ) for most regions, and for those regions we use  $n_e = 100 \text{ cm}^{-3}$  since the derived abundances are almost independent of density in this case (Osterbrock & Ferland 2006). For the other regions we find values of  $n_e$  that go up to  $4300 \text{ cm}^{-3}$ . Table A1 shows the densities obtained from each diagnostic in our sample objects.

We derive the electron temperatures using the line intensity ratios  $[\text{N II}] (\lambda 6548 + \lambda 6584)/\lambda 5755$  and  $[\text{O III}] (\lambda 4959 + \lambda 5007)/\lambda 4363$  to calculate  $T_e[\text{N II}]$  and  $T_e[\text{O III}]$ , respectively. The intensity of  $[\text{N II}] \lambda 5755$  can have a contribution from the recombination of  $\text{N}^{++}$  (Rubin 1986; Stasińska 2005), leading to an overestimate of the electron temperature that will affect the calculation of the chemical abundances. We can estimate this contribution using the formula derived by Liu et al. (2000), which provides an estimate of the contribution of recombination to the intensity of  $[\text{N II}] \lambda 5755$  that depends on  $T_e$  and the  $\text{N}^{++}/\text{H}^+$  abundance ratio. We assume that  $\text{N}^+$  and  $\text{N}^{++}$  are the main ionization stages of nitrogen so that  $\text{N}^{++}/\text{H}^+ = \text{N}/\text{H} - \text{N}^+/\text{H}^+$  (see Section 3.3 below). We find that the contribution of recombination to the  $[\text{N II}] \lambda 5755$  line intensity is lower than 2 percent for the objects in our sample, implying differences in  $T_e[\text{N II}]$  lower than 200 K. Since these differences are below the uncertainties associated to this temperature, and since the correction

**Table 1.** Atomic data used in our calculations

Ion	Transition probabilities	Collision strengths
O <sup>+</sup>	Zeippen (1982), Wiese et al. (1996)	Pradhan et al. (2006), Tayal (2007)
O <sup>++</sup>	Storey & Zeippen (2000), Wiese et al. (1996)	Aggarwal & Keenan (1999)
N <sup>+</sup>	Galavis et al. (1997), Wiese et al. (1996)	Tayal (2011)
S <sup>+</sup>	Podobedova et al. (2009)	Tayal & Zatsarimny (2010)

is somewhat uncertain, we have not applied the correction by recombination to  $T_e[\text{N II}]$ .

### 3.2 Blends with the [O III] $\lambda 4363$ line

The [O III]  $\lambda 4363$  emission line can be blended with several lines in low-resolution spectra. Rodríguez & Delgado-Inglada (2011) explored the effect of this blending in a sample of five Galactic H II regions, finding that the contribution of blending can lead to values of  $T_e[\text{O III}]$  that are up to 1000 K higher and oxygen abundances that are up to 0.05 dex lower than those implied by the unblended line. Furthermore, Curti et al. (2017) found in stacked spectra of high-metallicity star-forming galaxies that the [O III]  $\lambda 4363$  emission line is severely blended with [Fe II]  $\lambda 4359$  and some other feature, and this blending can result in a value of  $T_e[\text{O III}]$  that is overestimated by up to a factor of 10.

In order to analyse how the contribution of other emission lines affects the determination of  $T_e[\text{O III}]$ , we have selected 24 H II regions of our sample where the spectral resolution of their deep spectra allows the measurement of several lines that are close to [O III]  $\lambda 4363$ . We also include in this sample the Galactic H II region NGC 2579 from Esteban et al. (2013) and TOL 1924-416 from Esteban et al. (2014), which are not included in our main sample because [N II]  $\lambda 5755$  is not detected in their observed spectra. Table 2 shows the intensities of [O III]  $\lambda 4363$ , [Fe II]  $\lambda 4359$ , O II  $\lambda 4367$  and O I  $\lambda 4368$  for these 26 H II regions. These lines will be blended with [O III]  $\lambda 4363$  at spectral resolutions larger than  $\sim 5 \text{ \AA}$ , like those used for the observations of most of our sample objects.

We have added the intensities of the lines listed in Table 2 to the intensity of [O III]  $\lambda 4363$  for the 26 H II regions of this sample. For 30 Doradus and M42 we also add the intensity of the S III  $\lambda 4362$  line, with values of  $I(\lambda)/I(\text{H}\beta) \times 100 = 0.0145 \pm 0.03$  and  $0.016 \pm 0.004$ , respectively, and for NGC 2579 we add the intensity of the N II  $\lambda 4361$  line, with a value of  $0.023 \pm 0.08$ . Table 2 provides for each region the value of  $T_e[\text{O III}]$ , the blended value of  $T_e[\text{O III}]$  implied by [O III]  $\lambda 4363_{\text{blended}}$ , the change in the oxygen abundance introduced by the blended  $T_e[\text{O III}]$ , and the degree of ionization measured as  $P = I([\text{O III}] \lambda 44959, 5007)/I([\text{O III}] \lambda 44959, 5007) + I([\text{O II}] \lambda 3727)$ .

The left panel of Fig. 1 shows the ratio between the original and blended value of [O III]  $\lambda 4363$  as a function of the degree of ionization,  $P$ , for the sample of 26 H II regions. We have plotted the sample with different symbols according to their values of  $T_e[\text{O III}]$  listed in column 7 of Table 2. The squares show objects with  $T_e[\text{O III}] \leq 8500 \text{ K}$ , the circles have  $8500 \text{ K} < T_e[\text{O III}] \leq 10000 \text{ K}$  and the triangles represent objects with  $T_e[\text{O III}] > 10000 \text{ K}$ . We find that, as expected, the objects with low degree of ionization and low temperatures are the ones more affected by the blending.

In these 26 objects of our sample, the contribution of the [Fe II], O II, and O I lines goes up to 40 per cent of the intensity that would be measured for the [O III]  $\lambda 4363$  feature at low spectral resolution.

The blending leads to differences of up to 1000 K in  $T_e[\text{O III}]$  and up to 0.08 dex in O/H in the sample objects. The differences in O/H will be clearly larger for low-ionization, high-metallicity objects, especially if there is no measurement of  $T_e[\text{N II}]$  so that  $T_e[\text{O III}]$  (or the value of  $T_e[\text{N II}]$  inferred from  $T_e[\text{O III}]$  and a temperature relation) is used to derive the O<sup>+</sup> abundance. On the other hand, for objects with  $T_e[\text{O III}] > 10^4 \text{ K}$ , the differences between  $T_e[\text{O III}]$  and the blended  $T_e[\text{O III}]$  are lower than 130 K, and the maximum differences in O/H are equal to 0.01 dex. Hence, the effects of blending can be safely discarded for these objects (see Table 2).

We have fitted a straight line with the least-squares method to the data in the left panel of Fig. 1 to determine a formula to correct  $T_e[\text{O III}]$  for the effects of blending. We excluded from the fit those objects with  $T_e[\text{O III}] > 10000 \text{ K}$ , since they require very small corrections and do not follow well the trend defined by the other objects. We obtain the following correction:

$$\frac{[\text{O III}] \lambda 4363}{[\text{O III}] \lambda 4363_{\text{blended}}} = 0.47(\pm 0.06)P + 0.56(\pm 0.05), \quad (1)$$

where [O III]  $\lambda 4363_{\text{blended}}$  is the intensity of the blended feature and [O III]  $\lambda 4363$  is the unblended intensity.

Since the effect of blending in [O III]  $\lambda 4363$  depends on both the degree of ionization and the temperature, we have also fitted the values of  $\Delta t \times t_{\text{blended}}^2$  as a function of  $P$ , where  $t = T_e[\text{O III}]/10^4 \text{ K}$  and  $\Delta t = t_{\text{unblended}} - t_{\text{blended}}$  for those objects with  $T_e[\text{O III}] < 10000 \text{ K}$ . The right panel of Fig. 1 shows the fit to the data provided by the least-squares method. We obtain the following equation to correct  $T_e[\text{O III}]$ :

$$\Delta t \times t_{\text{blended}}^2 = 0.093(\pm 0.011)P - 0.090(\pm 0.008). \quad (2)$$

The fit in Equation (2) yields a better correction for the blended  $T_e[\text{O III}]$  than the one provided by Equation (1). Equation (1) gives differences between the unblended and the corrected values that go up to 300 K in  $T_e[\text{O III}]$  and 0.04 dex in O/H, whereas Equation (2) leads to differences that only go up to 200 K and 0.03 dex in O/H.

On the other hand, the corrections implied by Equation (2) depend on the atomic data used in the calculations. However, different combinations of transition probabilities and collision strengths for O<sup>++</sup> lead to very similar results. For example, the transition probabilities of Froese Fischer & Tachiev (2004) and the collision strengths of Storey et al. (2014) imply  $\Delta t \times t_{\text{blended}}^2 = 0.094(\pm 0.012)P - 0.091(\pm 0.008)$ .

We use Eq. 2 to correct the values of  $T_e[\text{O III}]$  for those H II regions in our main sample that have  $T_e[\text{O III}] < 10^4 \text{ K}$  and low spectral resolution ( $\geq 5 \text{ \AA}$ ). The differences between the measured and corrected  $T_e[\text{O III}]$  range from 200

**Table 2.** The values of the intensities of [O III]  $\lambda$ 4363, [Fe II]  $\lambda$ 4359, O II  $\lambda$ 4367, and O I  $\lambda$ 4368 with respect to  $H\beta = 100$ , and the values calculated for the measured and blended  $T_e[\text{O III}]$ , the differences and metallicity,  $\Delta\log(\text{O}/\text{H})$ , and the  $P$  parameter for a sample of 26 H II regions with spectra of high spectral resolution.

ID	Region	[O III] $\lambda$ 4363	[Fe II] $\lambda$ 4359	O II $\lambda$ 4367	O I $\lambda$ 4368	$T_e[\text{O III}]$ (K) (measured)	$T_e[\text{O III}]$ (K) (blended)	$\Delta\log(\text{O}/\text{H})$	$P$	Ref.
5	30 Doradus	3.209±0.05	0.0285±0.004	0.0245±0.004	0.0211±0.003	9900 ± 100	9900	0.00	0.85	1
7	IC 211*	1.51±0.07	0.041±0.009	0.025±0.007	0.044±0.009	9200 ± 100	9300	0.02	0.60	2
9	N11B*	1.48±0.06	0.023±0.002	0.027±0.002	0.022±0.002	9100 ± 100	9200	0.01	0.65	2
10	N44C*	6.8±0.5	0.010±0.002	0.039±0.004	–	11300 ± 300	11300	0.00	0.93	2
11	NGC 1714*	2.5±0.1	–	0.034±0.008	0.021±0.007	9500 ± 100	9600	0.01	0.82	2
62	HH202	0.944±0.085	0.060±0.009	0.025±0.005	0.082±0.012	8100 ± 200	8500	0.05	0.74	3
65	M8	0.286±0.011	0.041±0.005	0.015±0.004	0.052±0.006	8000 ± 100	8700	0.03	0.38	4
66	M16	0.192±0.02	–	–	0.122±0.015	7600 ± 200	8600	0.04	0.28	5
67	M17	0.953±0.05	–	0.030±0.012	0.022±0.009	7900 ± 100	8000	0.02	0.83	4
69	M20	0.148±0.02	0.063±0.017	–	0.027±0.011	7700 <sup>+200</sup> <sub>-300</sub>	8700	0.03	0.20	5
70	M42	1.301±0.026	0.058±0.006	0.048±0.005	0.073±0.007	8300 ± 100	8600	0.05	0.86	6
–	NGC 2579	1.877±0.094	–	0.041±0.010	0.037±0.010	9300 ± 200	9500	0.02	0.81	7
75	NGC 3576	1.279±0.03	0.051±0.006	0.0409±0.006	0.069±0.006	8400 ± 100	8700	0.04	0.78	8
77	NGC 3603	2.483±0.12	–	–	0.116±0.046	9000 ± 100	9100	0.02	0.92	5
81	S311	0.562±0.02	0.026±0.009	0.092±0.012	0.039±0.010	8900 ± 100	9600	0.03	0.32	9
90	NGC 2363	13.7±0.5	0.028±0.007	–	–	16000 ± 300	16000	0.00	0.97	10
98	VS 44	0.62±0.06	0.12±0.04	–	0.10±0.04	8200 ± 200	8900	0.08	0.66	10
123	HII1	6.70±0.23	0.103±0.023	–	0.068±0.019	11900 ± 200	12000	0.01	0.86	11
124	HII2	6.46±0.23	0.067±0.027	–	0.019±0.008	11800 ± 200	11900	0.01	0.85	11
126	UV1	3.95±0.16	0.099±0.031	–	0.037±0.015	10800 ± 200	11000	0.01	0.77	11
127	NGC 5408	12.0±0.5	0.07±0.01	–	0.07±0.01	15500 ± 400	15500	0.00	0.90	12
143	N66	6.26±0.626	0.050±0.020	–	–	12600 ± 500	12400	0.00	0.85	13
144	N66A*	5.1±0.1	0.034±0.004	–	0.025±0.004	12500 ± 200	12500	0.00	0.75	2
145	N81*	6.8±0.3	0.027±0.001	0.021±0.001	0.028±0.002	12700 ± 200	12800	0.01	0.87	2
146	N88A*	13.0±1.0	0.088±0.005	0.015±0.002	0.117±0.007	14900 ± 500	15000	0.01	0.95	2
–	TOL 1924-416	9.4±0.4	0.13±0.03	–	0.09±0.03	13500 ± 300	13600	0.01	0.86	12

References for the line intensities: (1) Peimbert (2003), (2) Toribio San Cipriano et al. (2017), (3) Mesa-Delgado et al. (2009), (4) García-Rojas et al. (2007), (5) García-Rojas et al. (2006), (6) Esteban et al. (2004), (7) Esteban et al. (2013), (8) García-Rojas et al. (2004), (9) García-Rojas et al. (2005), (10) Esteban et al. (2009), (11) López-Sánchez et al. (2007), (12) Esteban et al. (2014), (13) Tsamis et al. (2003). \* The intensities of [Fe II]  $\lambda$ 4359, O II  $\lambda$ 4367, and O I  $\lambda$ 4368 for these regions are reported by Domínguez-Guzmán et al. (in preparation).

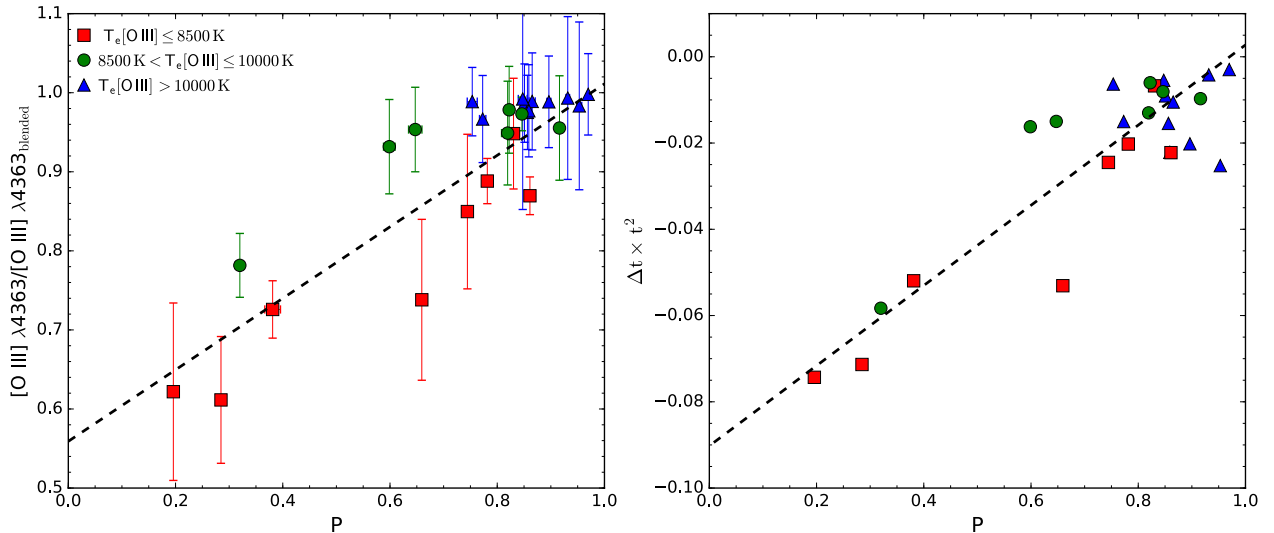


**Figure 1.** Left: the [O III]  $\lambda$ 4363/[O III]  $\lambda$ 4363<sub>blended</sub> intensity ratio as a function of the degree of ionization for a sample of 26 H II regions. Right: temperature correction given by  $\Delta t \times t^2$  as a function of the degree of ionization. The symbols in both panels are for three different ranges of  $T_e[\text{O III}]$ ; squares for regions with  $T_e[\text{O III}] \leq 8500$  K, circles for regions with  $8500 \text{ K} < T_e[\text{O III}] \leq 10000$  K, and triangles for regions with  $T_e[\text{O III}] > 10000$  K. The dashed lines in both plots show our fits for objects with  $T_e[\text{O III}] \leq 10^4$  K (squares and circles).

K to 1270 K, and the differences in metallicity from 0.02 dex to 0.14 dex. The final results for  $T_e[\text{O III}]$  and  $T_e[\text{N II}]$  are reported in Table A1 in Appendix A.

### 3.3 Ionic and total abundances

We calculate the ionic oxygen abundances using the intensity ratios of  $[\text{O II}] \lambda 3727$  and  $[\text{O III}] (\lambda 4959 + \lambda 5007)$  with respect to  $\text{H}\beta$ . We adopt a two-zone ionization structure characterized by  $T_e[\text{N II}]$  in the  $[\text{O II}]$  emitting region and by  $T_e[\text{O III}]$  in the  $[\text{O III}]$  emitting region. Adding the contribution from both ions we obtain the total oxygen abundance:  $\text{O}/\text{H} = \text{O}^+/\text{H}^+ + \text{O}^{++}/\text{H}^+$ . The total nitrogen abundance is calculated using the intensity of  $[\text{N II}] (\lambda 6548 + \lambda 6584)$  and the assumption that  $\text{N}/\text{O} \approx \text{N}^+/\text{O}^+$  (Peimbert & Costero 1969), which seems to be working well according to Delgado-Inglada et al. (2015). We report the results of the oxygen abundances and the N/O abundance ratios in the eighth and ninth columns of Table A1. Note that for four H II regions, NGC 604, NGC 2363, NGC 5461, and NGC 5471, studied by Esteban et al. (2002), it was not possible to calculate the oxygen and nitrogen abundances, since  $[\text{O II}] \lambda 3727$  was outside the spectral range of their observations.

## 4 THE $T_e[\text{N II}]-T_e[\text{O III}]$ RELATION

### 4.1 Final sample

Fig. 2 shows the relation between  $T_e[\text{N II}]$  and  $T_e[\text{O III}]$  for the whole sample of H II regions. The solid and dashed lines show the temperature relations of Campbell, Terlevich & Melnick (1986) and Pagel et al. (1992), respectively, which will be discussed below. We identify with stars the Galactic H II regions and with different symbols the results for NGC 2363 and NGC 5471. These objects are giant H II regions located in the irregular galaxy NGC 2366 (NGC 2363) and the spiral galaxy M101 (NGC 5471). The squares show the results obtained for NGC 5471 with the observations of Luridiana et al. (2002), Esteban et al. (2002), Kennicutt, Bresolin & Garnett (2003), and Croxall et al. (2016), and the triangles show the results for NGC 2363 based on the spectra of Esteban et al. (2002) and Esteban et al. (2009). The observations of Luridiana et al. (2002) and Kennicutt et al. (2003) for NGC 5471 and Esteban et al. (2002) for NGC 2363 lead to values of  $T_e[\text{N II}]$  that are much higher than those implied by other observations of these objects.

We have examined the behaviour of the regions with high values of  $T_e[\text{N II}]$  in diagrams that involve the intensity ratios of  $[\text{O III}]$ ,  $[\text{N II}]$ ,  $[\text{S II}]$ , and  $[\text{O I}]$  lines relative to H I lines. These diagrams are generally used to separate H II regions from regions affected by other sources of excitation, like shocks (see, e.g., Allen et al. 2008). We find that the regions with high  $T_e[\text{N II}]$  do not depart from the bulk of the other regions in these diagrams.

We have also carried out echelle spectroscopic observations of NGC 5471 and NGC 2363 to explore if these high values of  $T_e[\text{N II}]$  might be due to observational problems or related to some other physical process, such as the presence of high-density regions (Morisset 2017) or shocks. Our main conclusion is that at least some of these high values of  $T_e[\text{N II}]$

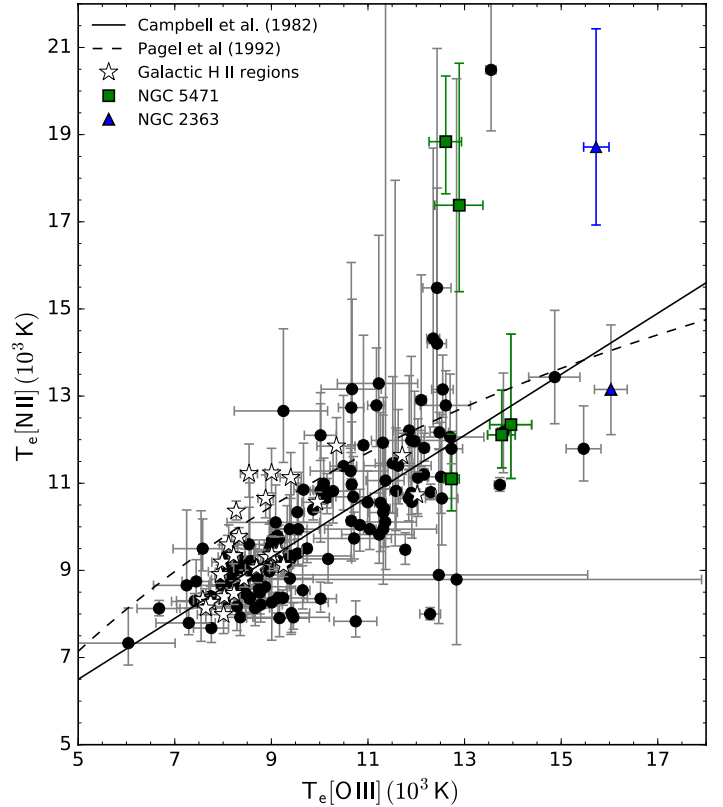


**Figure 2.** Values of  $T_e[\text{N II}]$  as a function of  $T_e[\text{O III}]$  for a sample of 168 spectra of 133 H II regions collected from the literature. The stars identify Galactic H II regions. Squares and triangles show the results for NGC 5471 and NGC 2363, respectively. The solid and dashed lines represent the temperature relations of Campbell et al. (1986) and Pagel et al. (1992), respectively.

are real, in the sense of not being due to observational problems, but they do not provide a representative temperature of the  $[\text{N II}]$  and  $[\text{O II}]$  emitting regions (Arellano-Córdova et al., in preparation). Therefore, we have discarded from the sample H II regions with  $T_e[\text{N II}] > 16000$  K.

We have also removed those regions with temperature uncertainties larger than 30 percent. With these selection criteria, our final sample comprises 154 observations of 124 H II regions.

### 4.2 The dispersion in the $T_e[\text{N II}]-T_e[\text{O III}]$ relation

The large dispersion in the  $T_e[\text{N II}]-T_e[\text{O III}]$  relation has been reported previously for smaller samples in other studies (e.g. Pérez-Montero & Contini 2009; Berg et al. 2015; Croxall et al. 2016, and references therein). Part of this dispersion might be related to observational problems since  $[\text{O III}] \lambda 4363$  and  $[\text{N II}] \lambda 5755$  are relatively weak lines. As commented above, the high values of  $T_e[\text{N II}]$  found in some regions can be due to high-density regions or shocks. The degree of ionization can also contribute to this dispersion as we discuss in Sections 4.3 and 4.4 below.

Ercolano, Bastian & Stasińska (2007) have studied the dispersion in the relation between  $T_e[\text{O II}]$  and  $T_e[\text{O III}]$  using photoionization models with different spatial distributions

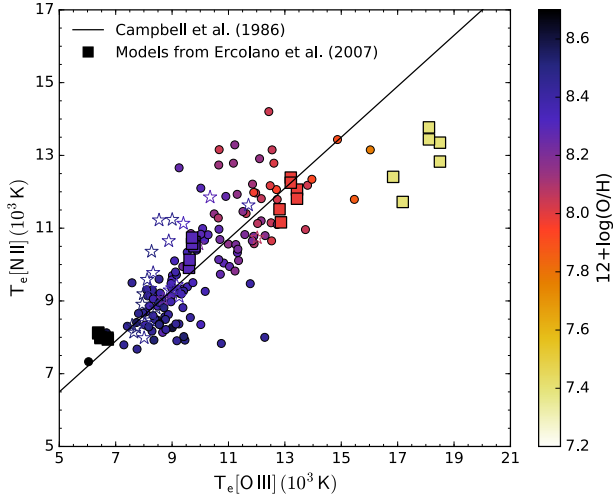


**Figure 3.** Values of  $T_e[\text{N II}]$  as a function of  $T_e[\text{O III}]$  for our sample of 154 observations of 124 H II regions collected from the literature. The squares show the photoionization models calculated by Ercolano et al. (2007). The solid line shows the temperature relation of Campbell et al. (1986). The symbols are grey-coded (colour-coded in the online version) with the metallicity. The stars identify Galactic H II regions.

of the ionizing sources and different metallicities. They conclude that part of the dispersion in the  $T_e[\text{O II}]-T_e[\text{O III}]$  relation is due to metallicity. Fig. 3 shows the relation between  $T_e[\text{N II}]$  and  $T_e[\text{O III}]$  as a function of the metallicity (grey or colour-coded) for our sample of H II regions. The range in metallicity in our sample goes from  $12 + \log(\text{O}/\text{H}) = 7.78$  to 8.84. We have also plotted with squares the models of Ercolano et al. (2007) for different geometries and metallicities. Fig. 3 shows the expected metallicity dependence of the temperature relation. The photoionization models of Ercolano et al. (2007) are broadly consistent with our results. The models of lower metallicity show a shift to lower values of  $T_e[\text{N II}]$ . This reflects the dependence of the different processes of cooling on the metallicity. For instance, cooling due to collisional excitation of H I can be important at low metallicities (Péquignot 2008). The amount of  $\text{H}^0$  will depend on the density structure and this could also introduce dispersion in the temperature relation. On the other hand, the different temperatures of the ionizing sources might also contribute to the dispersion of the temperature relation, as argued by Pilyugin et al. (2010a).

### 4.3 Temperature relations from the literature

Campbell et al. (1986) [see also Garnett (1992)] proposed a temperature relation based on photoionization models of Stasińska (1982), which is widely used in the literature and is parametrized as:

$$T_e[\text{N II}] \approx T_e[\text{O II}] = 0.7 T_e[\text{O III}] + 3000 \text{ K}. \quad (3)$$

Another temperature relation is the one proposed by Pagel et al. (1992), which is based on photoionization models of Stasińska (1990):

$$t_{2,\text{O}}^{-1} = 0.5(t_{3,\text{O}}^{-1} + 0.8), \quad (4)$$

where  $t_{2,\text{O}} = T_e[\text{O II}]/10^4 \text{ K}$  and  $t_{3,\text{O}} = T_e[\text{O III}]/10^4 \text{ K}$ . Fig. 2 shows the temperature relations from Campbell et al. (1986) and Pagel et al. (1992) in solid and dashed lines respectively.

Pérez-Montero & Díaz (2003) proposed a temperature relation based on photoionization models that includes the dependence of  $T_e[\text{O II}]$  on density,  $n_e$  (see also Hägele et al. 2006; Pérez-Montero 2017). This temperature relation is:

$$t_{2,\text{O}} = \frac{1.2 + 0.002n_e + 4.2/n_e}{t_{3,\text{O}}^{-1} + 0.08 + 0.003n_e + 2.5/n_e}, \quad (5)$$

The bottom panel of Fig. 4 shows this temperature relation for four different values of density (10, 100, 500, and 1000  $\text{cm}^{-3}$ ) represented with different lines. Our results (grey-coded with density, or colour-coded in the online version of this figure) show that there is no clear dependence with the density.

Other relations between temperatures have been proposed using observational data. Esteban et al. (2009) derive a temperature relation based on a sample of H II regions with deep spectra, which is very similar to the one obtained by Campbell et al. (1986) (see also Esteban et al. 2017). Recently, Croxall et al. (2016) use a sample of H II regions from the M 101 galaxy, and also find a relation very similar to the one proposed by Esteban et al. (2009) and Campbell et al. (1986).

Pilyugin (2007) uses a sample of H II regions to propose a temperature relation with a dependence on the  $P$  parameter. However, for most of the regions used by Pilyugin (2007) it was not possible to measure  $[\text{N II}] \lambda 5755$ , and this author used an empirical expression to estimate the value of this line. The temperature relation proposed by Pilyugin (2007) is:

$$\frac{1}{t_{2,\text{N}}} = 0.41 \frac{1}{t_{3,\text{O}}} - 0.34 P + 0.81, \quad (6)$$

where  $t_{2,\text{N}} = T_e[\text{N II}]/10^4 \text{ K}$ . The top panel of Fig. 4 shows the temperature relation of Pilyugin (2007) for different values of the  $P$  parameter (0.3, 0.6, and 0.9) along with our sample, grey/colour-coded with the  $P$  parameter. It can be seen that many H II regions do not follow this temperature relation.

Some of these temperature relations are widely used in the literature, but their performance has been little studied. Our sample of H II regions with measurements of both  $T_e[\text{N II}]$  and  $T_e[\text{O III}]$  allows us to compare these relations to the observational data and to study how their use affects the determination of chemical abundances (see Section 5 below).

### 4.4 Temperature relations from this work

Fig. 5 shows again the relation between  $T_e[\text{N II}]$  and  $T_e[\text{O III}]$  for our final sample, grey/colour-coded with the value of the  $P$  parameter. The solid line shows the temperature relation of Campbell et al. (1986), which we will use for comparison purposes. The results in Fig. 5 illustrate that the  $T_e[\text{N II}]-T_e[\text{O III}]$  relation has a dependence on the degree of ionization, a result previously found by Pilyugin (2007) for a small number of H II regions.

We have used robust fits to obtain a new set of temperature relations that depend on this parameter. The purpose of robust fits is to minimize the effect of outliers. We use this approach because the uncertainties in the line intensities reported by the different authors have not been estimated in

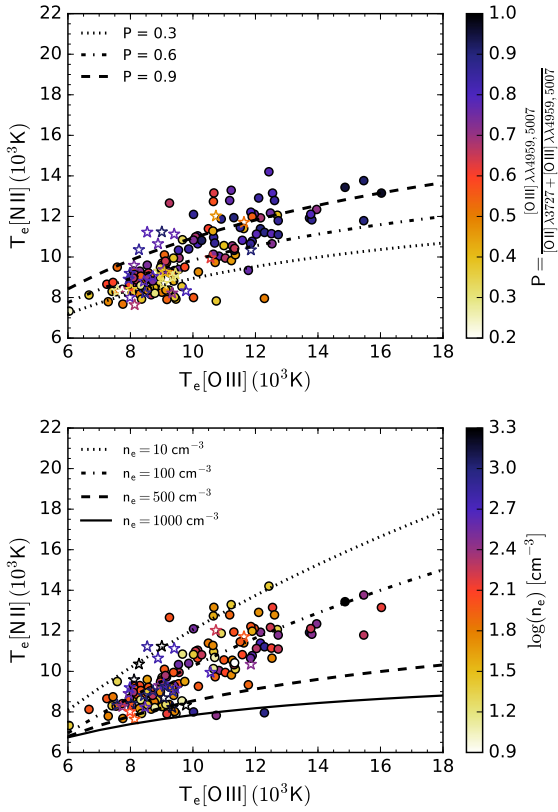


**Figure 4.** Values of  $T_e[\text{N II}]$  as a function of  $T_e[\text{O III}]$  for our sample of 154 observations of 124 H II regions collected from the literature. Top panel: The temperature relation of Pilyugin (2007). The symbols are grey/colour-coded with the  $P$  parameter, and the lines are for different values of the  $P$  parameter. Bottom panel: The temperature relation of Pérez-Montero & Díaz (2003). The symbols are grey/colour-coded with density, and the lines show the relation for different values of density. The stars identify Galactic H II regions.

a homogenous way, and we suspect that some of them may have been underestimated. On the other hand, since some of the Galactic H II regions depart from the trend defined by extragalactic objects, maybe because their spectra cover a small region of the nebula, we have discarded these regions in our calculations. We have separated our sample in two ranges of  $P$ ,  $P < 0.5$  and  $P \geq 0.5$ , and propose two temperature relations to estimate either  $T_e[\text{N II}]$  or  $T_e[\text{O III}]$  for each range of  $P$ . For  $P < 0.5$ :

$$\frac{1}{t_2} = 0.54(\pm 0.07) \frac{1}{t_3} + 0.52(\pm 0.08), \quad (7)$$

$$\frac{1}{t_3} = 1.04(\pm 0.14) \frac{1}{t_2} - 0.05(\pm 0.15), \quad (8)$$

and for  $P \geq 0.5$ :

$$\frac{1}{t_2} = 0.61(\pm 0.04) \frac{1}{t_3} + 0.36(\pm 0.04), \quad (9)$$

$$\frac{1}{t_3} = 1.00(\pm 0.07) \frac{1}{t_2} + 0.03(\pm 0.07), \quad (10)$$

where  $t_2 = T_e[\text{N II}]/10^4$  K and  $t_3 = T_e[\text{O III}]/10^4$  K. Fig 5 shows these fits (Eqs. 7–10) plotted with dotted (for  $P < 0.5$ ) and dashed lines (for  $P \geq 0.5$ ).

## 5 EFFECTS OF THE $T_E[\text{N II}]-T_E[\text{O III}]$ RELATION ON THE O/H, N/H AND N/O ABUNDANCE RATIOS.

We study the effect of using the temperature relations in the determination of chemical abundances for the set of relations derived here and for four other relations from the literature described in Section 4.3 (Campbell et al. 1986; Pagel et al. 1992; Pérez-Montero & Díaz 2003; Pilyugin 2007). We calculate the differences between the abundances calculated using the different temperature relations to estimate either  $T_e[\text{N II}]$  from  $T_e[\text{O III}]$  or  $T_e[\text{O III}]$  from  $T_e[\text{N II}]$ , and the abundances calculated using the measurements of both  $T_e[\text{N II}]$  and  $T_e[\text{O III}]$ . The results are shown below for the sample of 154 spectra of 124 H II regions, excluding four objects observed by Esteban et al. (2002) since their spectra do not include measurements of [O II] lines.

Fig. 6 shows the differences in O/H, N/H and N/O obtained with the temperature relations of Pagel et al. (1992); Pilyugin (2007); Pérez-Montero & Díaz (2003); Campbell et al. (1986), and the relations from this work. The dark/blue symbols show the abundance differences implied by the use of  $T_e[\text{O III}]$  to estimate  $T_e[\text{N II}]$  and the grey/red symbols show the differences when we use  $T_e[\text{N II}]$  to estimate  $T_e[\text{O III}]$ . We also show with empty stars the results for the Galactic H II regions.

The results for O/H (left panels) and N/H (middle panels) are very similar. This is an expected result since the total nitrogen abundance is derived using  $\text{N}/\text{H} = \text{O}/\text{H} \times \text{N}/\text{O}$ , and  $\text{N}/\text{O} = \text{N}^+/\text{O}^+$  is calculated using  $T_e[\text{N II}]$  and a line ratio of collisionally excited lines whose emissivities have similar dependences on the electron temperature. In general, the temperature relations perform well when the temperature relation is used to estimate  $T_e[\text{N II}]$  from the value of  $T_e[\text{O III}]$  (dark/blue symbols in Fig. 6). The exception is the relation of Pagel et al. (1992), that leads to higher differences from the abundances obtained using both temperatures and a dependence of the results with the  $P$  parameter. The second column of Table 3 provides the mean and standard deviation of the differences implied by the different relations when  $T_e[\text{N II}]$  is estimated from  $T_e[\text{O III}]$  (the results for the Galactic H II regions have not been included in these calculations). It can be seen that in this case the temperature relations of Pilyugin (2007), the ones derived here, and the one of Campbell et al. (1986) are performing better than the others.

On the other hand, the temperature relations perform worse when they are used to estimate  $T_e[\text{O III}]$  from  $T_e[\text{N II}]$  (grey/red symbols and the third column in Table 3). The relation of Pagel et al. (1992) leads to abundances that are systematically higher by about 0.2 dex. The relation of Pérez-Montero & Díaz (2003) does not work for 13 H II regions in the sample that have relatively high densities,  $n_e \geq 500$   $\text{cm}^{-3}$ , and results in very low abundances for some regions with high  $P$ . The temperature relation of Pilyugin (2007) introduces a large dispersion in the resulting abundances.

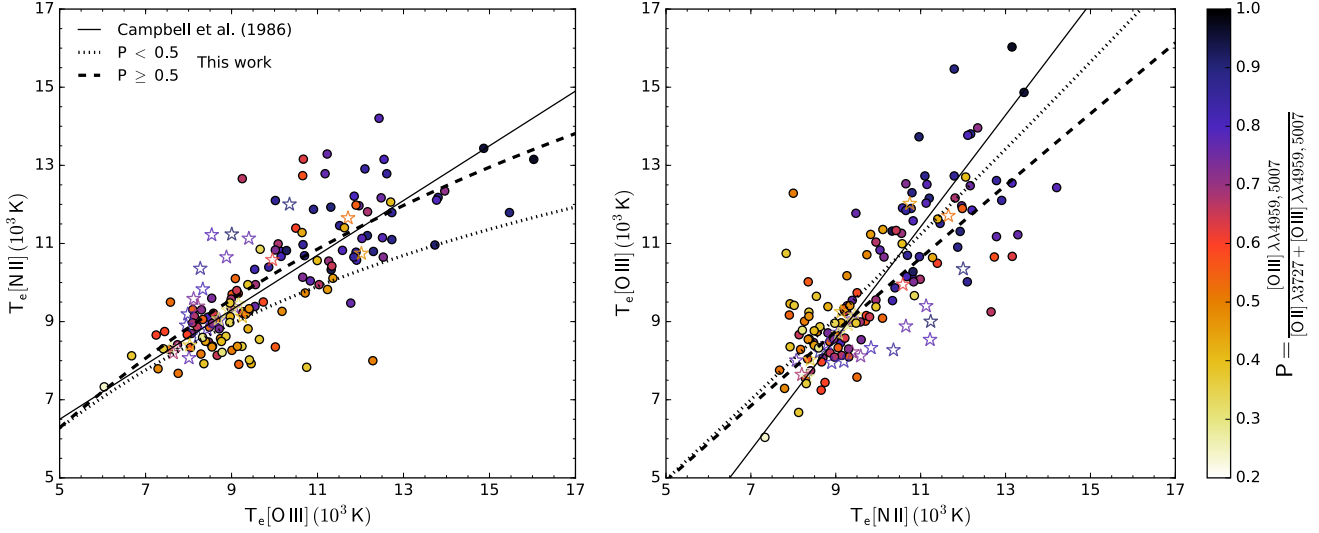


**Figure 5.** Values of  $T_e[\text{N II}]$  as a function of  $T_e[\text{O III}]$  and viceversa for our sample of 154 observations of 124 H II regions collected from the literature. The symbols are grey/colour-coded with the  $P$  parameter. Dashed lines show the temperature relations proposed in this work. Left panel: fits from Eqs. 7 for  $P < 0.5$  (dotted line) and 9 for  $P \geq 0.5$  (dashed line). Right panel: fits from Eqs. 8 (dotted line) for  $P < 0.5$  and 10 for  $P \geq 0.5$  (dashed line). The solid line shows the temperature relation of Campbell et al. (1986). The stars identify the Galactic H II regions in our sample, which were discarded from the fits.

**Table 3.** Mean and dispersion of the oxygen abundance differences for the temperature relations from the literature and from this work.

Temperature relation	$T_e[\text{O III}] \rightarrow T_e[\text{N II}]$	$T_e[\text{N II}] \rightarrow T_e[\text{O III}]$
	$\Delta \log(\text{O}/\text{H})$	$\Delta \log(\text{O}/\text{H})$
Campbell et al. (1986)	$-0.02 \pm 0.10$	$0.00 \pm 0.11$
Pagel et al. (1992)	$-0.10 \pm 0.12$	$+0.18 \pm 0.16$
Pérez-Montero & Díaz (2003)	$-0.02 \pm 0.09$	$-0.03 \pm 0.14$
Pilyugin (2007)	$-0.01 \pm 0.09$	$+0.02 \pm 0.18$
This work	$-0.01 \pm 0.10$	$0.00 \pm 0.09$

The relation from Campbell et al. (1986) and, especially, the relations derived here, work much better in this case.

In summary, the temperature relation of Campbell et al. (1986) is the one performing better from the relations available in the literature, and the relations presented in this work improve slightly on this relation. An inspection of Fig. 3, suggests that our relations will probably work better than the relation of Campbell et al. (1986) for objects with lower metallicities than the ones considered here.

## 6 THE EFFECT OF USING A SINGLE VALUE OF TEMPERATURE

In some studies, chemical abundances are calculated using a single value of temperature, either  $T_e[\text{N II}]$  or  $T_e[\text{O III}]$ , to characterize the whole nebula (e.g., Stanghellini et al. 2010). We can use our sample of both temperatures to analyse the effect of using either  $T_e[\text{N II}]$  or  $T_e[\text{O III}]$  in the derived abundances. Fig. 7 shows the differences between the oxygen abundances calculated using either  $T_e[\text{N II}]$  (right panel) or  $T_e[\text{O III}]$  (left panel) and the oxygen abundances calculated using both temperatures plotted as a function of the  $P$  parameter.

The effect of using a single value of the temperature will not be large if  $T_e[\text{O III}]$  is most easily measured in re-

gions with high  $P$ , where  $\text{O}^{++}$  dominates the determination of the total oxygen abundance, and if  $T_e[\text{N II}]$  is the temperature most easily obtained for regions where the ion  $\text{O}^+$  prevails. We have used the observed, uncorrected for extinction, intensities of  $[\text{O III}] \lambda 4363$  and  $[\text{N II}] \lambda 5755$  in our sample of H II regions to get an idea of which of these lines would be easier to observe if the spectra had lower quality. We can do that for 129 observations of 107 H II regions in our sample, where the observed intensities are reported in the original studies or can be obtained from the extinction-corrected values using the same extinction law and the values of  $c(\text{H}\beta)$  provided there. Fig. 7 shows those H II regions where the observed intensity for  $[\text{O III}] \lambda 4363$  is larger than the one observed for  $[\text{N II}] \lambda 5755$  with grey/green symbols (left panel) and the regions where the observed intensity of  $[\text{N II}] \lambda 5755$  is larger than the one observed for  $[\text{O III}] \lambda 4363$  with grey/magenta symbols (right panel). The empty circles in each plot of Fig. 7 show those H II regions where it was not possible to obtain the observed intensities of  $[\text{O III}] \lambda 4363$  and  $[\text{N II}] \lambda 5755$  because the information required to do so was not provided. We also show with empty stars the Galactic H II regions.

The results presented in Fig. 7 show that it is indeed possible to find H II regions with a low degree of ionization where  $T_e[\text{O III}]$  is most easily measured and vice versa, regions with a high degree of ionization where  $T_e[\text{N II}]$  is the



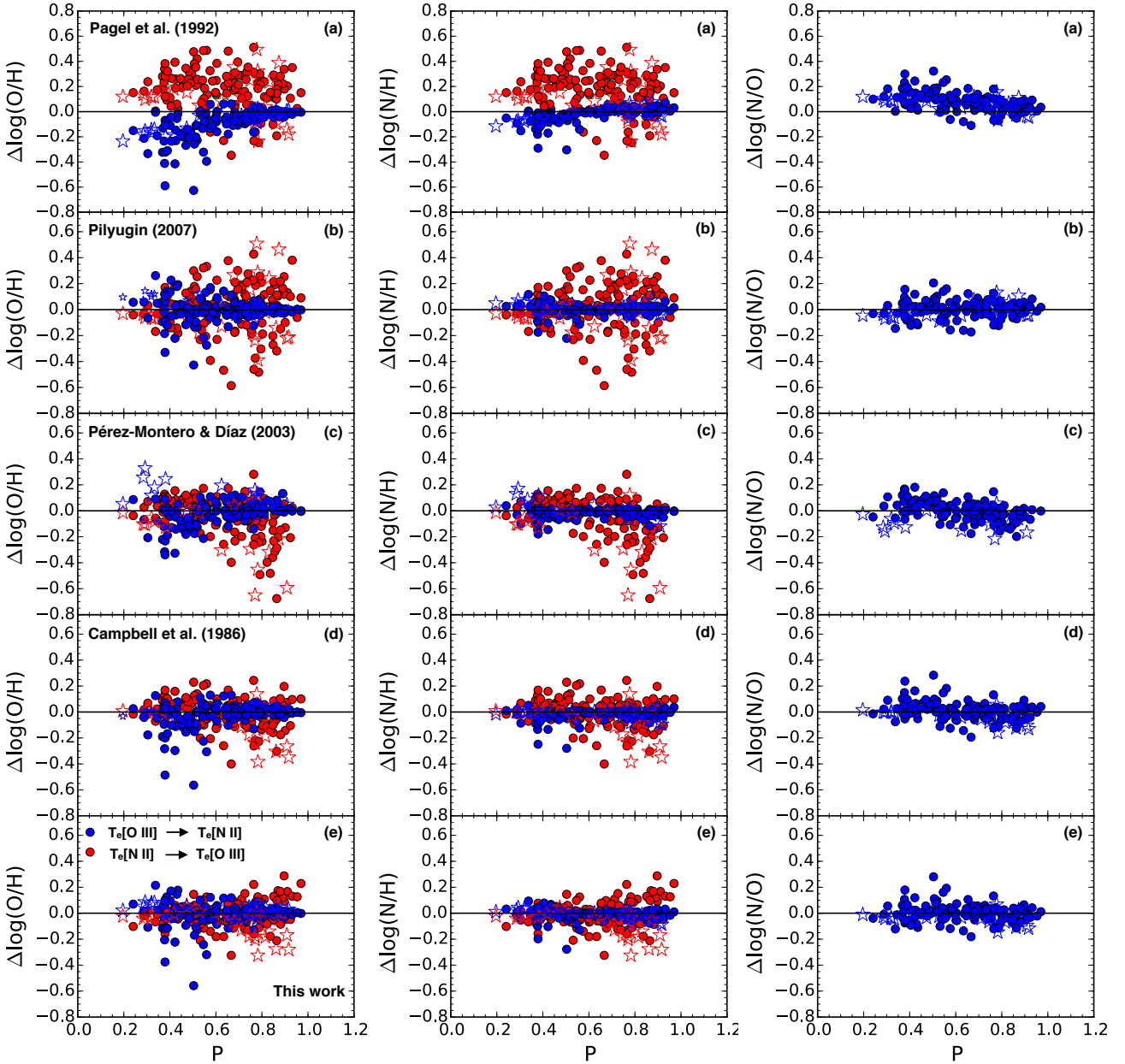


**Figure 6.** Differences between the O/H, N/H, and N/O abundances calculated using different temperature relations and those calculated using both  $T_e[\text{N II}]$  and  $T_e[\text{O III}]$ . The results are plotted as a function of the  $P$  parameter. The temperature relations are: (a) Pagel et al. (1992), (b) Pilyugin (2007), (c) Pérez-Montero & Díaz (2003), (d) Campbell et al. (1986), and (e) this work. Dark/blue symbols show the differences when we estimate  $T_e[\text{N II}]$  from  $T_e[\text{O III}]$ ; grey/red symbols those obtained when we estimate  $T_e[\text{O III}]$  from  $T_e[\text{N II}]$ . The stars identify the Galactic H II regions.

only temperature that will be measured. Fig. 7 also shows that the differences in the oxygen abundances introduced by the use of a single temperature can be significant. The largest differences might be due to unrealistically high or low values of  $T_e[\text{N II}]$  or  $T_e[\text{O III}]$ . For example, the largest differences are found for He 2-10 and +131.9+18.5 in NGC 628, two objects that have values of  $T_e[\text{O III}]$  much higher than those obtained for  $T_e[\text{N II}]$  (see Table A1) and that depart significantly from the  $T_e[\text{N II}]-T_e[\text{O III}]$  relation defined by the bulk of objects. However, the results for the other objects show that the differences in the oxygen abundances can easily reach 0.2 dex.

We have also calculated the differences in N/H and N/O introduced by the use of a single value of temperature. For the N/H abundance, in most of the objects we find differences of up to 0.1 dex when we use  $T_e[\text{O III}]$ , and differences of up to 0.38 dex when  $T_e[\text{N II}]$  is used. Since the  $\text{N}^+$  and  $\text{O}^+$  ions are localized in the low ionization zone of the nebula, these ions are characterized by  $T_e[\text{N II}]$ . Therefore, we only calculate the differences for the N/O abundance ratios when the value of  $T_e[\text{O III}]$  is used. Our results show differences in N/O that go up to 0.2 dex.

In order to decide whether it is better to use a single

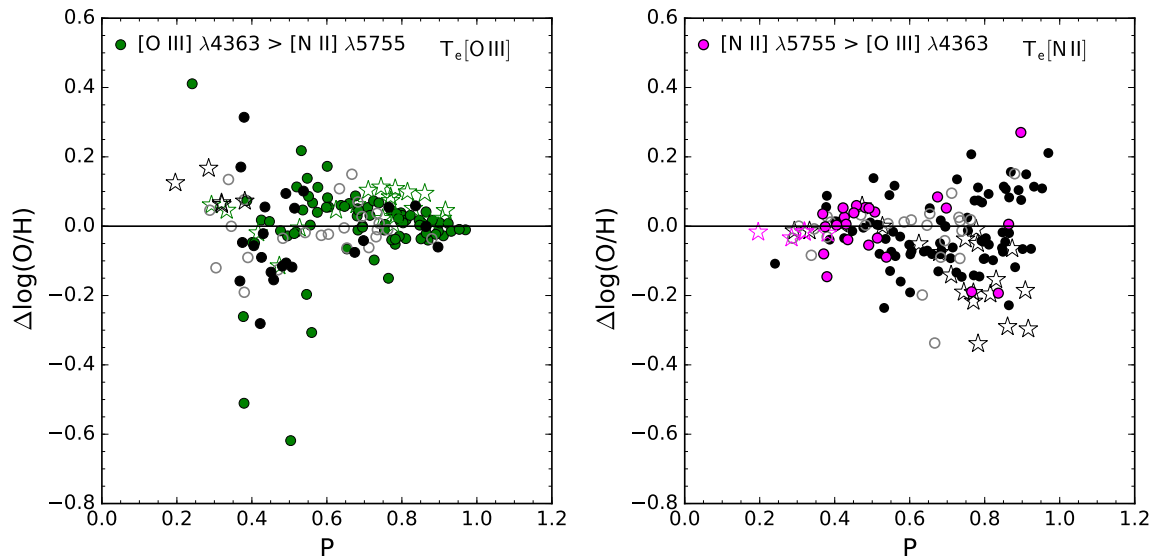


**Figure 7.** Oxygen abundance differences versus the  $P$  parameter. Left panel: differences between the metallicity calculated using only  $T_e[\text{O III}]$  and the one based on both temperatures. Grey/green circles show 101 regions where the observed intensity of  $[\text{O III}] \lambda 4363$  is larger than the one of  $[\text{N II}] \lambda 5755$ . Right panel: differences between the metallicity derived using only  $T_e[\text{N II}]$  and the one calculated with both temperatures. Grey/magenta circles show 27 regions where the observed intensity of  $[\text{N II}] \lambda 5755$  is larger than the one of  $[\text{O III}] \lambda 4363$ . The empty circles show those regions where it was not possible to obtain the observed intensities (uncorrected for extinction) of the  $[\text{N II}] \lambda 5755$  and  $[\text{O III}] \lambda 4363$  lines. The stars identify the Galactic H II regions.

value of temperature or to use a temperature relation to estimate a second value, we can compare the results presented in Fig. 7 with those shown in the left panel of Fig. 6(e) and Table 3. If the value of  $T_e[\text{O III}]$  is used to do all the calculations, using  $T_e[\text{O III}]$  to derive  $T_e[\text{N II}]$  with the temperature relations derived here is better, since it leads to lower deviations. On the other hand, if  $T_e[\text{N II}]$  is the reference temperature, the improvement introduced by the use of the temperature relations to infer  $T_e[\text{O III}]$  is smaller, though it still leads to somewhat lower deviations.

## 7 THE DIRECT METHOD VERSUS THE R, S, ONS, C, O3N2, AND N2 STRONG-LINE METHODS

The sample of H II regions with measurements of  $T_e[\text{N II}]$  and  $T_e[\text{O III}]$  allows us to analyse the performance and reliability of strong-line methods. To do that, we compare the metallicities calculated using some strong-line methods with the metallicities implied by the direct method. We have selected some of the more commonly used strong-line methods whose calibration is based on observational data: the ONS method of Pilyugin et al. (2010b), the C method of Pilyugin et al. (2012a), the O3N2 and N2 methods calibrated by Marino et al. (2013), and the R and S methods of Pilyugin & Grebel (2016).

The O3N2 and N2 methods are based on relations between the O/H abundance ratio and the line intensity ratios  $O3N2 = ([\text{O III}] \lambda 5007/\text{H}\beta) \times (\text{H}\alpha/[\text{N II}] \lambda 6584)$  and  $N2 = ([\text{N II}] \lambda 6584/\text{H}\alpha)$ , respectively. We use the calibrations of Marino et al. (2013) for these methods, which are valid for  $-1.1 < O3N2 < 1.7$  and  $-1.6 < N2 < -0.2$  or, equiva-

lently, for  $12 + \log(\text{O}/\text{H}) \geq 8.0$ . Marino et al. (2013) estimate uncertainties of 0.18 dex for the O3N2 method and 0.16 dex for the N2 method.

The ONS and C methods of Pilyugin et al. (2010b) and Pilyugin et al. (2012a) use the relative intensities of  $[\text{O II}] \lambda 3727$ ,  $[\text{O III}] \lambda 5007$ ,  $[\text{N II}] \lambda 6584$  and  $[\text{S II}] \lambda 6717, 6731$ , and  $\text{H}\beta$  to derive the abundances of O/H, N/H, and N/O, but each method uses a different approach. Both methods have estimated uncertainties lower than 0.1 dex.

The R method of Pilyugin & Grebel (2016) uses the relative intensities of  $[\text{O II}] \lambda 3727$ ,  $[\text{O III}] (\lambda 4959 + \lambda 5007)$ ,  $[\text{N II}] (\lambda 6548 + 84)$ , and  $\text{H}\beta$ , whereas their S method is based on the relative intensities of  $[\text{O III}] \lambda 5007$ ,  $[\text{N II}] \lambda 6584$ , and  $[\text{S II}] \lambda 6717, 6731$ , and  $\text{H}\beta$ . The differences in metallicity between the direct method and the R and S methods are reported to be less than 0.1 dex (Pilyugin & Grebel 2016).

Table A2, whose full version is available online, shows the oxygen abundances calculated using these strong-line methods (columns 5–10) for the regions in our final sample (defined in Section 4.1). We have excluded the Galactic H II regions from these calculations because their spectra are generally obtained in a small area that cannot be considered as representative of the whole object. For this reason, Galactic H II regions are not usually included in the calibration samples of strong-line methods (see, e.g., Pilyugin et al. 2012a). In order to ease the comparison between the methods, Table A2 also shows the results of the direct method (column 4). Note that it is not possible to calculate O/H with all the strong-line methods for some H II regions. In some cases, the regions are outside of the limits of validity of the O3N2 or N2 methods and, in the case of the H II regions observed by Esteban et al. (2002), no measurements of  $[\text{O II}]$  are provided.

Fig. 8 shows the differences between the oxygen abundances implied by the R, S, O3N2, N2, ONS, and C methods and those derived with the direct method, plotted as a function of the  $P$  parameter, and colour/grey-coded with the values of N/O and O/H. The circles show the results for our sample.

The results presented in Fig. 8 show that strong-line methods can lead to important departures from the oxygen abundances derived with the direct method, even though these methods have been calibrated using samples with temperature-based abundances. Some differences, especially those of the outliers, are likely due to observational problems, which will affect mostly the abundances obtained with the direct method (Arellano-Córdova et al. 2016). This is further explored in the next section.

### 7.1 Observational uncertainties

We can explore the effect of observational errors in the abundance determinations by comparing the results obtained with each method for those regions that have more than one observed spectra in our sample. Table 4 shows the results for the 12 objects that have two or more spectra, with column 1 listing the spectra identifications from Table A2, column 2 the number of spectra available for each region, column 3 the object identification, and columns 4 to 10 the ranges in O/H implied by the different methods. An inspection of the results presented in Table 4 shows that in most cases the direct method leads to wider metallicity ranges, as expected from its higher sensitivity to observational problems.

However, there are objects for which the direct method is providing more consistent results than the other methods. This behaviour is found for NGC 456 in Table 4. This is an extended H II region of the Small Magellanic Cloud, and it is possible that the spectra available for this nebula are not representative of the emission of the entire region. There are other regions in the sample like, e.g., 30 Doradus, that also have large angular sizes, but since there is no clear-cut way to decide which regions are too extended to be analyzed with strong-line methods, we have not excluded any of these regions.

An estimate of the uncertainty introduced by observational problems in each method can be obtained from the root mean square of the differences in O/H implied by each pair of spectra for the objects listed in Table 4. The 31 spectra of the 12 objects identified in this table lead to 32 pairs for each method, with the exception of the O3N2 and N2 methods that have 18 and 22 pairs, respectively. The estimated observational uncertainties are equal to 0.11 dex for the direct method, and in the range 0.06–0.16 dex for the strong-line methods, with the C and ONS methods showing the highest dispersions, 0.15–0.16 dex. These large dispersions are introduced by the results for NGC 456. If we exclude this region from the calculations we find observational errors of 0.13 dex for the direct method and in the range 0.05–0.07 dex for the strong-line methods.

We have calculated for each strong-line method the root mean square value of the differences in O/H relative to the direct method. For a sample of 126 spectra, we find standard deviations of 0.17 dex for the R and ONS methods, 0.16 dex for the S method, and 0.14 dex for the C method. We could use the O3N2 and N2 methods in a sample of 86 and 111

extragalactic H II region spectra from our sample, respectively, and the standard deviations based on these regions are 0.16 dex in both cases. The observational uncertainties estimated above can only explain part of these dispersions. We explore in the next sections whether problems with the sample selection can explain the trends with  $P$ , N/O, and O/H shown by the differences in Fig. 8.

### 7.2 The relation between N/O and O/H

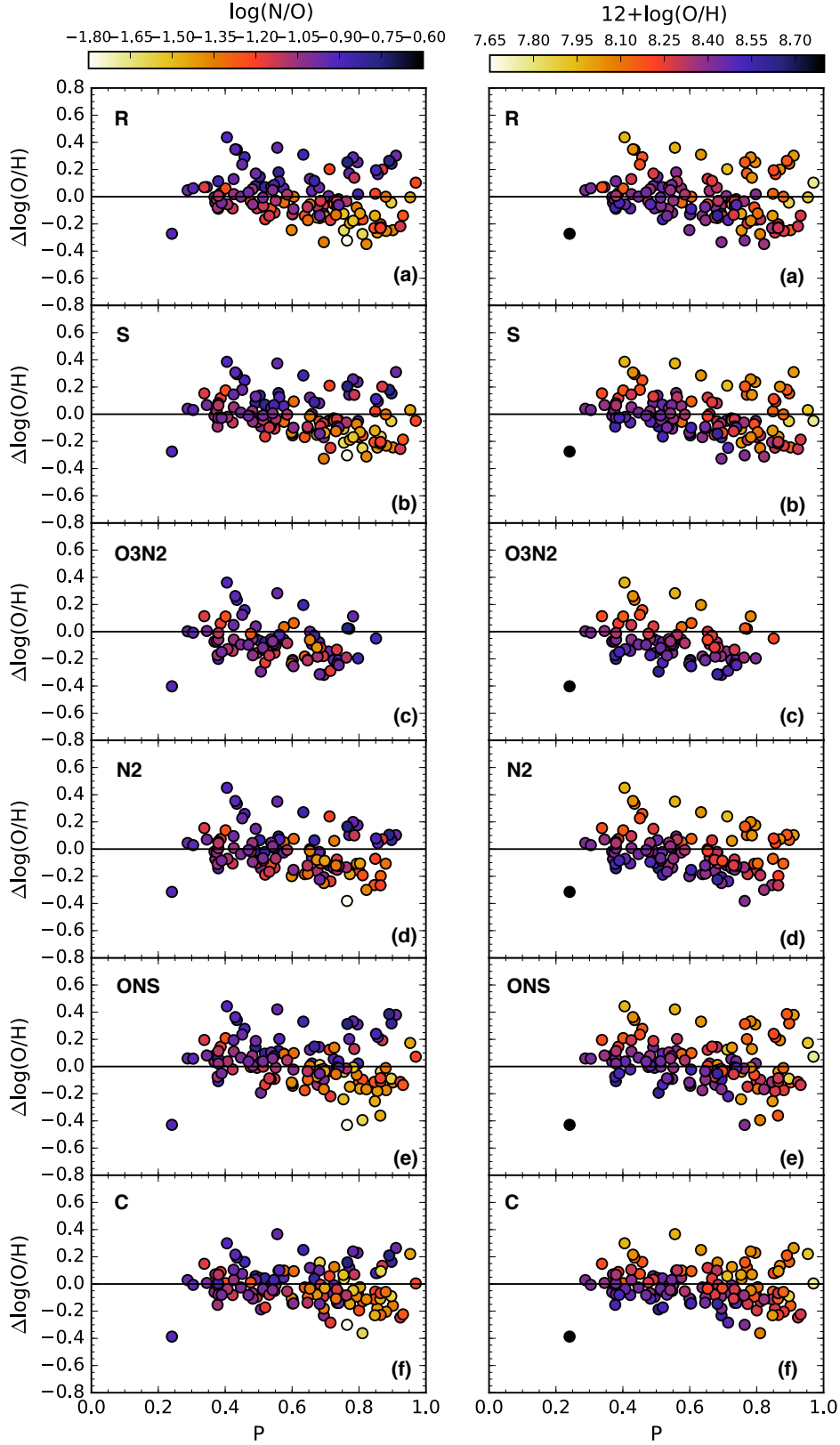
The left panels of Fig. 8 show the dependence on N/O of the departures of the values of O/H obtained with the strong-line methods from the values derived with the direct method. This is not a surprising result since the O3N2, N2, ONS, and C methods all use the [N II] lines in their calibration and all of them implicitly assume that for a given value of O/H, N/O is fixed or varies within a small range (see Vale Asari et al. 2016), which is not necessarily true (Garnett 1990; Pérez-Montero 2014). The dependence of the differences on O/H (shown in the left panels of Figs. 8 and 10) was also to be expected, since it reflects that the assumptions necessarily made by strong-line methods work in different ways at different metallicities.

Fig. 9 shows the values of N/O as a function of O/H for the H II regions in our sample. The results in Fig. 9 show the well-known dispersion in the values of N/O at a given O/H. We do not know if this dispersion is real or due to observational problems. If the dispersion arises from observational problems, one could assume that selecting those objects that lead to a lower dispersion would be equivalent to selecting those objects that have the best observed spectra.

In order to explore this idea, we have selected a subsample of nebular spectra that follow closely the N/O-O/H relation generally assumed by strong-line methods (see, e.g., Pilyugin et al. 2012b). These are the 89 results represented with filled symbols in Fig. 9, and Fig. 10 plots for these spectra the differences in O/H between strong-line methods and the direct method as a function of O/H and  $P$ . The results are only presented for the R, N2, and C methods, since the other methods do not have very different behaviour.

The standard deviations of the differences plotted in Fig. 10 are in the range 0.11–0.14 dex. These dispersions are somewhat lower than the ones shown by the full sample in Fig. 8, but the differences still display very similar behaviour in both figures. In addition, we identify with overlapping symbols in Fig. 9 those regions with uncertainties lower than 0.1 dex in both N/O and O/H. The analysis of this sample leads to the same behaviour as our previous results for the differences in O/H as a function of  $P$ . This result supports the idea that the trends shown by the strong-line methods with respect to the direct method are not due to observational problems. Besides, it also rules out that they are introduced by departures of the sample objects from the N/O-O/H relation assumed by strong-line methods (Vale Asari et al. 2016).

The dispersion in the N/O versus O/H diagram might also be introduced by N enrichment of the observed nebulae by the winds of Wolf-Rayet (W-R) stars. We have identified with diamonds those objects whose spectra have W-R features in Figs. 9 and Fig. 10. The H II regions with W-R features follow the distribution of the other objects in these figures, but they seem to form a large fraction of those ob-



**Figure 8.** Differences between the oxygen abundances obtained with strong-line methods and those implied by the direct method. The differences are plotted as a function of the  $P$  parameter, colour/grey-coded with the N/O abundance ratio (left) and O/H (right). Panels (a) to (f) show the results of the R, S, O3N2, N2, ONS, and C methods. The circles show our sample of extragalactic H II regions with measurements of both  $T_e[N II]$  and  $T_e[O III]$ .

**Table 4.** Metallicity ranges obtained with the direct, R, S, ONS, C, O3N2 and N2 methods for H II regions with two or more spectra in our sample.

ID	N	Region	$12 + \log(\text{O}/\text{H})$						
			$T_e$	R	S	ONS	C	O3N2	N2
5–6	2	30 Doradus	8.30 – 8.36	8.07 – 8.13	8.09 – 8.16	8.21 – 8.25	8.23 – 8.25	–	8.03 – 8.10
8–9	2	N11B	8.39 – 8.40	8.07 – 8.21	8.07 – 8.28	8.23 – 8.29	8.29 – 8.29	8.18 <sup>†</sup>	8.15 – 8.21
31–32	2	H143	8.04 – 8.33	8.35 – 8.35	8.32 – 8.33	8.37 – 8.38	8.28 – 8.29	8.24 – 8.25	8.31 – 8.33
33–34	2	H149	8.26 – 8.44	8.36 – 8.38	8.34 – 8.35	8.40 – 8.41	8.30 – 8.30	8.23 – 8.23	8.32 – 8.33
43–45	3	H1013	8.34 – 8.60	8.35 – 8.52	8.41 – 8.55	8.46 – 8.58	8.41 – 8.52	8.33 – 8.40	8.39 – 8.46
49–53	5	NGC 5461	8.42 – 8.56	8.34 – 8.47	8.37 – 8.44	8.44 – 8.50	8.33 – 8.39	8.24 – 8.35	8.29 – 8.43
54–55	2	NGC 5471	7.93 – 8.15	8.13 – 8.15	8.14 – 8.15	8.06 – 8.14	7.99 – 8.09	–	8.04 – 8.17
95–96	2	VS 38	8.28 – 8.48	8.39 – 8.41	8.40 – 8.42	8.40 – 8.46	8.40 – 8.40	8.28 – 8.34	8.28 – 8.37
97–98	2	VS 44	8.36 – 8.41	8.34 – 8.40	8.36 – 8.37	8.38 – 8.41	8.34 – 8.36	8.27 – 8.28	8.30 – 8.33
140–141	2	SHOC 011	8.06 – 8.14	8.31 – 8.35	8.28 – 8.32	8.34 – 8.39	8.26 – 8.30	8.16 – 8.17	8.24 – 8.26
143–144	2	N66	8.00 – 8.02	7.88 – 7.88	7.89 – 7.90	7.76 – 7.76	7.79 – 8.07	–	–
147–151	5	NGC 456	8.02 – 8.08	7.79 – 7.97	7.82 – 7.98	7.69 – 8.16	7.72 – 8.21	–	8.03 – 8.08 <sup>‡</sup>

NOTE. † and ‡ identify results based on just one (†) or two (‡) spectra.

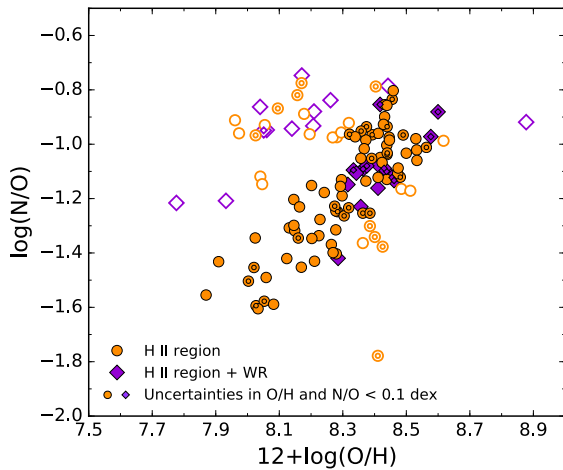


**Figure 9.** N/O abundances ratios as a function of O/H for our sample of extragalactic H II regions with measurements of both  $T_e[\text{N II}]$  and  $T_e[\text{O II}]$ . The diamonds show the H II regions with W-R features. The empty symbols represent those regions that were discarded from the calculations described in Section 7.2, and the overlapping small symbols indicate those regions with abundance uncertainties lower than 0.1 dex in both O/H and N/O.

jects with  $\log(\text{N}/\text{O}) \approx -0.9$ . This suggests that the structure at  $\log(\text{N}/\text{O}) \approx -0.9$  in the N/O-O/H diagram in Fig. 9 might be real and attributable to N enrichment by W-R stars.

We have checked whether the structure at  $\log(\text{N}/\text{O}) \approx -0.9$  in the N/O-O/H diagram could be due to any kind of problem affecting the values of  $T_e[\text{N II}]$  or  $T_e[\text{O II}]$  by recalculating the N/O and O/H abundance ratios using just one of these temperatures (with or without a temperature relation to define the other). In all cases, the results are very similar to those shown in Fig. 9, but with larger dispersion, which suggests that the structure is difficult to explain with some kind of temperature anomaly.

If further observations of high quality show that the structure at  $\log(\text{N}/\text{O}) \approx -0.9$  in the N/O-O/H diagram is real and related to W-R stars, this would mean that strong-line methods that assume a tight relation between N/O and O/H should not be used to analyze H II regions that are associated to W-R stars.

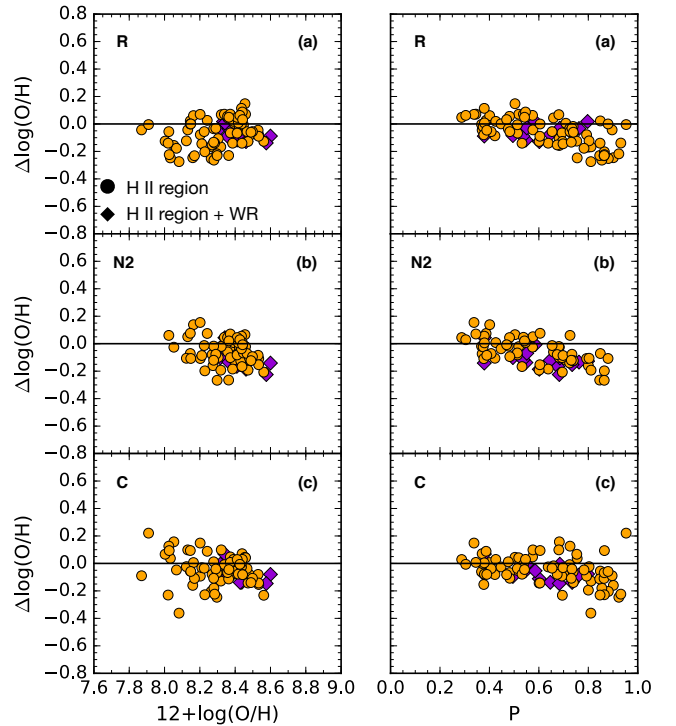


**Figure 10.** Differences between the oxygen abundances obtained with some strong-line methods and those implied by the direct method for those objects represented with filled symbols in Fig. 9. The differences are plotted as a function of metallicity (left panels) and the P parameter (right panels). Panels (a) to (c) show the results of the R, N2, and C methods. The diamonds show objects that have W-R features.

### 7.3 The trend with P

Fig. 8 shows that the oxygen abundance differences depend on the degree of ionization in a similar way. This suggests that this dependence might be due to the procedure we follow to calculate the physical conditions and chemical abundances with the direct method. In order to check whether this is true, we have recalculated the physical conditions and oxygen abundances with the direct method following the same procedure used by Pilyugin et al. (2012a) for the

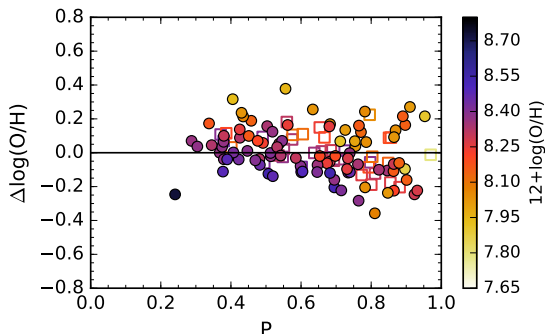


**Figure 11.** Differences between the oxygen abundances implied by the C method and those calculated with the direct method following the procedure and atomic data used by Pilyugin et al. (2012a) in their calibration of the C method. The results are shown as a function of the  $P$  parameter, and are colour-coded with metallicity. The circles show our sample and the squares show those regions in common to the calibration sample of the C method.

calibration of the C method, which is similar to the procedures used by Pilyugin et al. (2010b) for the ONS method, Marino et al. (2013) for the O3N2 and N2 methods, and Pilyugin & Grebel (2016) for the R and S methods. We use the expressions provided by Pilyugin et al. (2012a), in the low density regime ( $n_e \leq 100 \text{ cm}^{-3}$ ), which are based on different atomic data than the ones used here, to calculate new values for  $T_e[\text{N II}]$ ,  $T_e[\text{O III}]$  and O/H for our sample of H II regions. Furthermore, we do not apply the correction for blending to the values of  $T_e[\text{O III}]$ . When we compare these new determinations with our previous results, we find differences lower than 400 K in  $T_e[\text{N II}]$  and 100 K in  $T_e[\text{O III}]$  for most of the objects in our sample. In the case of O/H, we find differences lower than 0.06 dex.

We now calculate the differences in the oxygen abundances implied by the C method and those newly derived with the direct method using the procedure of Pilyugin et al. (2012a). Fig. 11 shows these differences as a function of  $P$  and colour-coded with the new oxygen abundances obtained with the direct method. The symbols are the same as in Fig. 8, except that the squares show the regions of our sample that are also present in the calibration sample of the C method. A comparison between Fig. 11 and the right panel of Fig. 8(e) shows that the new results are very similar to the previous ones; they have a similar dispersion and the same dependence on the degree of ionization. We note that the highest differences in O/H are found in regions not included in the calibration sample of the C method. Pilyugin et al. (2012a) restricted their sample and the abundances assigned to each region using different criteria. If these criteria led to a selection of the spectra less affected by observational problems, the uncertainties of the abundances provided by the C method might be lower than the ones we find here, but we note that there is no guarantee of that being the case.

Since the dependence on  $P$  of the differences in O/H implied by most of these strong-line methods is not introduced by the procedure we use to determine O/H with the direct method nor by those regions that depart from the general trend in the N/O-O/H relation in Fig. 9, what is

the reason of this dependence? We think that it is due to the presence in the calibration samples of regions where the values measured for  $T_e[\text{N II}]$  were used to estimate  $T_e[\text{O III}]$  with the temperature relation of Campbell et al. (1986). The results presented in the left panel of Fig. 6(d) show that a similar dependence on  $P$  is found when O/H is calculated with this procedure. In fact, if we recalculate all the O/H abundance ratios with the direct method following this approach, the dependence of the differences on  $P$  disappears (and the dispersion of the results increases). This result suggests that the performance of the strong-line methods could be improved by avoiding the use in the calibration samples of objects whose abundances are only based on  $T_e[\text{N II}]$ .

## 8 SUMMARY AND CONCLUSIONS

We have compiled a sample of 154 observations of 124 H II regions with measurements of both  $T_e[\text{N II}]$  and  $T_e[\text{O III}]$  to study different problems related to chemical abundance determinations, such as the use of temperature relations and the reliability of strong-line methods.

We have analysed the contribution of blending with other lines to the intensity of the temperature-sensitive [O III]  $\lambda 4363$  line in low-resolution spectra using a sample of H II regions with deep, high-resolution spectra. We find that H II regions of low degree of ionization and high metallicity are the ones most affected by blending. We calculate two relations, Equations (1) and (2), that can be used to correct for this effect in objects with  $T_e[\text{O III}] < 10000$  K when the spectral resolution is  $\geq 5 \text{ \AA}$ .

We explore with our sample the behaviour of the  $T_e[\text{N II}]-T_e[\text{O III}]$  temperature relation. This relation, as previously reported with smaller samples, shows a large dispersion from a linear relation. Part of this dispersion is due to observational problems, related to the measurement of the faint, temperature-sensitive, [O III]  $\lambda 4363$  and [N II]  $\lambda 5755$  lines, but the dispersion is also due to departures introduced by metallicity and the degree of ionization. We propose new  $T_e[\text{N II}]-T_e[\text{O III}]$  relations that take into account those effects, given by Equations (7)–(10).

We analyse the effect of using several  $T_e[\text{N II}]-T_e[\text{O III}]$  temperature relations from the literature and our new relations in the calculation of oxygen and nitrogen abundances. To do so, we calculate the differences between the chemical abundances based on the temperature relations and those calculated with both electron temperatures, and analyse their means and dispersions. The temperature relation proposed by Campbell et al. (1986) and, especially, the relations from this work provide the best results, but the differences introduced by the use of these relations can easily reach 0.2 dex in O/H and N/H. On the other hand, the use of a single temperature, leads to even larger differences.

We also study the performance and reliability of the R, S, ONS, C, O3N2, and N2 strong-line methods, using our sample of objects to compare the metallicities implied by these methods with the ones calculated with the direct method. We find that the differences in O/H introduced by these methods can easily reach or surpass  $\pm 0.2$  dex, and the differences depend on metallicity, N/O, and the degree of ionization of the objects. These dependences will introduce biases when strong-line methods are used to compare the

metallicities of H II regions with different characteristics or to estimate galactic abundance gradients.

Our results allow us to stress the importance of obtaining more deep, well-calibrated spectra of H II regions, that have good spectral resolution, in order to have better estimates of temperatures and chemical abundances. We also recommend a careful use of the strong-line methods, one that takes into account all their biases and uncertainties.

## ACKNOWLEDGEMENTS

We thank two anonymous referees for comments that have helped us to improve the manuscript. We acknowledge support from Mexican CONACYT grant CB-2014-240562. KZA-C acknowledges support from Mexican CONACYT in both Ph. D. and postdoctoral grants 364239.

## DATA AVAILABILITY

This research is based on data available in the literature.

## REFERENCES

- Aggarwal K. M., Keenan F. P., 1999, *APJS*, **123**, 311
- Allen M. G., Groves B. A., Dopita M. A., Sutherland R. S., Kewley L. J., 2008, *ApJS*, **178**, 20
- Arellano-Córdova K. Z., Rodríguez M., Mayya Y. D., Rosa-González D., 2016, *MNRAS*, **455**, 2627
- Berg D. A., Skillman E. D., Garnett D. R., Croxall K. V., Marble A. R., Smith J. D., Gordon K., Kennicutt Jr. R. C., 2013, *ApJ*, **775**, 128
- Berg D. A., Skillman E. D., Croxall K. V., Pogge R. W., Moustakas J., Johnson-Groh M., 2015, *ApJ*, **806**, 16
- Bresolin F., 2007, *ApJ*, **656**, 186
- Bresolin F., Gieren W., Kudritzki R.-P., Pietrzyński G., Urbaneja M. A., Carraro G., 2009, *ApJ*, **700**, 309
- Campbell A., Terlevich R., Melnick J., 1986, *MNRAS*, **223**, 811
- Copetti M. V. F., Oliveira V. A., Riffel R., Castañeda H. O., Sanmartín D., 2007, *A&A*, **472**, 847
- Croxall K. V., Pogge R. W., Berg D. A., Skillman E. D., Moustakas J., 2016, *ApJ*, **830**, 4
- Curti M., Cresci G., Mannucci F., Marconi A., Maiolino R., Esposito S., 2017, *MNRAS*, **465**, 1384
- Deharveng L., Peña M., Caplan J., Costero R., 2000, *MNRAS*, **311**, 329
- Delgado-Inglada G., Rodríguez M., Peimbert M., Stasińska G., Morisset C., 2015, *MNRAS*, **449**, 1797
- Denicoló G., Terlevich R., Terlevich E., 2002, *MNRAS*, **330**, 69
- Ercolano B., Bastian N., Stasińska G., 2007, *MNRAS*, **379**, 945
- Espíritu J. N., Peimbert A., Delgado-Inglada G., Ruiz M. T., 2017, *RMxAA*, **53**, 95
- Esteban C., Peimbert M., Torres-Peimbert S., Rodríguez M., 2002, *ApJ*, **581**, 241
- Esteban C., Peimbert M., García-Rojas J., Ruiz M. T., Peimbert A., Rodríguez M., 2004, *MNRAS*, **355**, 229
- Esteban C., Bresolin F., Peimbert M., García-Rojas J., Peimbert A., Mesa-Delgado A., 2009, *ApJ*, **700**, 654
- Esteban C., Carigi L., Copetti M. V. F., García-Rojas J., Mesa-Delgado A., Castañeda H. O., Péquignot D., 2013, *MNRAS*, **433**, 382
- Esteban C., García-Rojas J., Carigi L., Peimbert M., Bresolin F., López-Sánchez A. R., Mesa-Delgado A., 2014, *MNRAS*, **443**, 624
- Esteban C., García-Rojas J., Pérez-Mesa V., 2015, *MNRAS*, **452**, 1553
- Esteban C., Mesa-Delgado A., Morisset C., García-Rojas J., 2016, *MNRAS*, **460**, 4038
- Esteban C., Fang X., García-Rojas J., Toribio San Cipriano L., 2017, *MNRAS*, **471**, 987
- Fernández-Martín A., Pérez-Montero E., Vílchez J. M., Mampaso A., 2017, *A&A*, **597**, A84
- Froese Fischer C., Tachiev G., 2004, *Atomic Data and Nuclear Data Tables*, **87**, 1
- Galavis M. E., Mendoza C., Zeppen C. J., 1997, *A&AS*, **123**
- García-Rojas J., Esteban C., Peimbert M., Rodríguez M., Ruiz M. T., Peimbert A., 2004, *ApJS*, **153**, 501
- García-Rojas J., Esteban C., Peimbert A., Peimbert M., Rodríguez M., Ruiz M. T., 2005, *MNRAS*, **362**, 301
- García-Rojas J., Esteban C., Peimbert M., Costado M. T., Rodríguez M., Peimbert A., Ruiz M. T., 2006, *MNRAS*, **368**, 253
- García-Rojas J., Esteban C., Peimbert A., Rodríguez M., Peimbert M., Ruiz M. T., 2007, *RMxAA*, **43**, 3
- Garnett D. R., 1990, *ApJ*, **363**, 142
- Garnett D. R., 1992, *AJ*, **103**, 1330
- Guseva N. G., Izotov Y. I., Stasińska G., Fricke K. J., Henkel C., Papaderos P., 2011, *A&A*, **529**, A149
- Hägele G. F., Pérez-Montero E., Díaz Á. I., Terlevich E., Terlevich R., 2006, *MNRAS*, **372**, 293
- Hägele G. F., Díaz Á. I., Terlevich E., Terlevich R., Pérez-Montero E., Cardaci M. V., 2008, *MNRAS*, **383**, 209
- Izotov Y. I., Thuan T. X., 2004, *ApJ*, **602**, 200
- Izotov Y. I., Thuan T. X., Lipovetsky V. A., 1997, *ApJS*, **108**, 1
- Juan de Dios L., Rodríguez M., 2017, *MNRAS*, **469**, 1036
- Kennicutt Jr. R. C., Bresolin F., Garnett D. R., 2003, *ApJ*, **591**, 801
- Kewley L. J., Ellison S. L., 2008, *ApJ*, **681**, 1183
- Kobulnicky H. A., Kewley L. J., 2004, *ApJ*, **617**, 240
- Liu X.-W., Storey P. J., Barlow M. J., Danziger I. J., Cohen M., Bryce M., 2000, *MNRAS*, **312**, 585
- López-Sánchez Á. R., Esteban C., García-Rojas J., Peimbert M., Rodríguez M., 2007, *ApJ*, **656**, 168
- Luridiana V., Esteban C., Peimbert M., Peimbert A., 2002, *RMxAA*, **38**, 97
- Luridiana V., Morisset C., Shaw R. A., 2015, *AAP*, **573**, A42
- Marino R. A., et al., 2013, *A&A*, **559**, A114
- McGaugh S. S., 1991, *ApJ*, **380**, 140
- Mesa-Delgado A., Esteban C., García-Rojas J., Luridiana V., Bautista M., Rodríguez M., López-Martín L., Peimbert M., 2009, *MNRAS*, **395**, 855
- Miralles-Caballero D., Rosales-Ortega F. F., Díaz A. I., Oti-Floranés H., Pérez-Montero E., Sánchez S. F., 2014, *MNRAS*, **445**, 3803
- Morisset C., 2017, in Liu X., Stanghellini L., Karakas A., eds, *IAU Symposium Vol. 323, Planetary Nebulae: Multi-Wavelength Probes of Stellar and Galactic Evolution*. pp 43–50 ([arXiv:1612.04242](https://arxiv.org/abs/1612.04242)), [doi:10.1017/S1743921317001004](https://doi.org/10.1017/S1743921317001004)
- Nazé Y., Rauw G., Manfroid J., Chu Y.-H., Vreux J.-M., 2003, *A&A*, **408**, 171
- Osterbrock D. E., Ferland G. J., 2006, *Astrophysics of Gaseous Nebulae and Active Galactic Nuclei*. University Science Books, Mill Valley, CA,
- Pagel B. E. J., Simonson E. A., Terlevich R. J., Edmunds M. G., 1992, *MNRAS*, **255**, 325
- Patterson M. T., Walterbos R. A. M., Kennicutt R. C., Chiappini C., Thilker D. A., 2012, *MNRAS*, **422**, 401
- Peña-Guerrero M. A., Peimbert A., Peimbert M., Ruiz M. T., 2012, *ApJ*, **746**, 115
- Peimbert A., 2003, *ApJ*, **584**, 735
- Peimbert M., Costero R., 1969, *Boletín de los Observatorios Tonantzintla y Tacubaya*, **5**, 3

- Péquignot D., 2008, *A&A*, **478**, 371  
 Pérez-Montero E., 2014, *MNRAS*, **441**, 2663  
 Pérez-Montero E., 2017, *PASP*, **129**, 043001  
 Pérez-Montero E., Contini T., 2009, *MNRAS*, **398**, 949  
 Pérez-Montero E., Díaz A. I., 2003, *MNRAS*, **346**, 105  
 Pilyugin L. S., 2007, *MNRAS*, **375**, 685  
 Pilyugin L. S., Grebel E. K., 2016, *MNRAS*, **457**, 3678  
 Pilyugin L. S., Thuan T. X., 2005, *ApJ*, **631**, 231  
 Pilyugin L. S., Vílchez J. M., Thuan T. X., 2006, *MNRAS*, **370**, 1928  
 Pilyugin L. S., Vílchez J. M., Cedrés B., Thuan T. X., 2010a, *MNRAS*, **403**, 896  
 Pilyugin L. S., Vílchez J. M., Thuan T. X., 2010b, *ApJ*, **720**, 1738  
 Pilyugin L. S., Grebel E. K., Mattsson L., 2012a, *MNRAS*, **424**, 2316  
 Pilyugin L. S., Grebel E. K., Mattsson L., 2012b, *MNRAS*, **424**, 2316  
 Podobedova L. I., Kelleher D. E., Wiese W. L., 2009, *Journal of Physical and Chemical Reference Data*, **38**, 171  
 Pradhan A. K., Montenegro M., Nahar S. N., Eissner W., 2006, *MNRAS*, **366**, L6  
 Rodríguez M., Delgado-Inglada G., 2011, *ApJL*, **733**, L50  
 Rubin R. H., 1986, *ApJ*, **309**, 334  
 Stanghellini L., Magrini L., Villaver E., Galli D., 2010, *A&A*, **521**, A3  
 Stasińska G., 1982, *A&AS*, **48**, 299  
 Stasińska G., 1990, *A&A*, **83**, 501  
 Stasińska G., 2005, *A&A*, **434**, 507  
 Stasińska G., 2010, in Bruzual G. R., Charlot S., eds, *IAU Symposium Vol. 262, Stellar Populations - Planning for the Next Decade*. pp 93–96 ([arXiv:0910.0175](https://arxiv.org/abs/0910.0175)), [doi:10.1017/S1743921310002590](https://doi.org/10.1017/S1743921310002590)  
 Stevenson C. C., 1994, *MNRAS*, **267**, 904  
 Storey P. J., Zeppen C. J., 2000, *MNRAS*, **312**, 813  
 Storey P. J., Sochi T., Badnell N. R., 2014, *MNRAS*, **441**, 3028  
 Tayal S. S., 2007, *ApJS*, **171**, 331  
 Tayal S. S., 2011, *ApJS*, **195**, 12  
 Tayal S. S., Zatsarinny O., 2010, *ApJS*, **188**, 32  
 Toribio San Cipriano L., García-Rojas J., Esteban C., Bresolin F., Peimbert M., 2016, *MNRAS*, **458**, 1866  
 Toribio San Cipriano L., Domínguez-Guzmán G., Esteban C., García-Rojas J., Mesa-Delgado A., Bresolin F., Rodríguez M., Simón-Díaz S., 2017, preprint, ([arXiv:1702.01120](https://arxiv.org/abs/1702.01120))  
 Tsamis Y. G., Barlow M. J., Liu X.-W., Danziger I. J., Storey P. J., 2003, *MNRAS*, **338**, 687  
 Vale Asari N., Stasińska G., Morisset C., Cid Fernandes R., 2016, *MNRAS*, **460**, 1739  
 Wiese W. L., Fuhr J. R., Deters T. M., 1996, *Journal of Physical and Chemical Reference Data*, Monograph 7, 403  
 Yates R. M., Schady P., Chen T.-W., Schweyer T., Wiseman P., 2019, arXiv e-prints,  
 Zeppen C. J., 1982, *MNRAS*, **198**, 111  
 Zurita A., Bresolin F., 2012, *MNRAS*, **427**, 1463

The full versions of Tables A1 and A2 are available on-line.

## APPENDIX A: TABLES

Table A1 lists the sample of 154 spectra of 124 H II regions, with our identification number (column 1), the galaxy where they are located and their name (columns 2 and 3), the values we derive for the electron density and temperature (columns 4 to 7), the values of O/H and N/H (columns 8 and 9), and the references for the spectra (column 10).

Table A2 shows the oxygen abundances calculated using the direct method and the R, S, ONS, C, O3N2, and N2 strong-line methods (columns 4–10) for the regions in our final sample (excluding the Galactic H II regions).



Table A1: Our calculated values for the electron densities, temperatures, oxygen abundances and nitrogen-to-oxygen abundance ratios for a sample of 154 observations of 124 H II regions compiled from the literature

ID	Galaxy	H II region	$n_e$ [S II] ( $\text{cm}^{-3}$ )	$n_e$ [O II] ( $\text{cm}^{-3}$ )	$T_e$ [O III] <sup>a</sup> (K)	$T_e$ [N II] (K)	12+log(O/H)	log(N/O)	Ref.
1	He 2-10	C	900 ± 100	–	12300 ± 200	8000 ± 100	8.46 <sup>+0.03</sup> <sub>-0.04</sub>	-0.83 <sup>+0.05</sup> <sub>-0.04</sub>	1
2	HS 0924+3821	–	< 100	–	12400 ± 200	14200 <sup>+3600</sup> <sub>-1800</sub>	8.04 ± 0.04	-1.12 <sup>+0.25</sup> <sub>-0.27</sub>	2
3	HS 1213+3636A	–	< 100	–	10700 ± 300	12700 <sup>+3300</sup> <sub>-1600</sub>	8.13 <sup>+0.09</sup> <sub>-0.08</sub>	-1.31 <sup>+0.28</sup> <sub>-0.31</sub>	2
4	J1253–0312	–	1200 ± 100	–	13700 ± 100	11900 ± 200	8.03 ± 0.01	-0.97 ± 0.03	1
5	LMC <sup>1</sup>	30 Doradus	400 ± 30	400 ± 20	9900 ± 100	10400 <sup>+300</sup> <sub>-200</sub>	8.36 ± 0.01	-1.25 ± 0.05	3
6	"	30 Doradus	300 ± 100	300 ± 100	10000 ± 300	12100 <sup>+700</sup> <sub>-600</sub>	8.30 ± 0.05	-1.19 ± 0.10	4
7	"	IC 2111	200 <sup>+200</sup> <sub>-100</sub>	200 ± 100	9200 ± 100	9700 ± 300	8.43 ± 0.03	-1.38 ± 0.07	5
8	"	N11B	100 ± 100	100 ± 50	9300 ± 300	9300 <sup>+400</sup> <sub>-300</sub>	8.40 ± 0.05	-1.34 <sup>+0.09</sup> <sub>-0.10</sub>	4
9	"	N11B	200 <sup>+200</sup> <sub>-100</sub>	200 ± 100	9100 ± 100	9800 ± 200	8.39 ± 0.02	-1.3 ± 0.06	5
10	"	N44C	200 <sup>+200</sup> <sub>-100</sub>	100 ± 100	11300 ± 300	10300 <sup>+500</sup> <sub>-400</sub>	8.28 ± 0.03	-1.25 ± 0.10	5
11	"	NGC 1714	400 ± 100	400 ± 100	9500 ± 100	10300 <sup>+700</sup> <sub>-500</sub>	8.36 ± 0.03	-1.36 ± 0.12	5
12	M31	17	< 100	–	7800 ± 400	7700 <sup>+400</sup> <sub>-300</sub>	8.46 ± 0.08	-0.80 ± 0.14	6
13	"	25	< 100	–	9000 ± 300	9400 ± 300	8.32 ± 0.05	-0.96 ± 0.09	6
14	"	26	< 100	–	9000 ± 500	9700 ± 400	8.32 <sup>+0.07</sup> <sub>-0.06</sub>	-0.92 ± 0.10	6
15	"	35	< 100	–	8500 ± 300	9600 <sup>+900</sup> <sub>-600</sub>	8.43 ± 0.06	-0.90 ± 0.17	6
16	"	K932	100 ± 100	200 ± 20	8300 ± 200	9300 ± 200	8.44 ± 0.03	-0.94 ± 0.05	7
17	M33	BCLMP 290	< 100	< 100	7600 ± 600	9500 <sup>+700</sup> <sub>-500</sub>	8.44 <sup>+0.13</sup> <sub>-0.10</sub>	-1.13 <sup>+0.14</sup> <sub>-0.15</sub>	8
18	"	BCLMP 626	< 100	< 100	9400 <sup>+1200</sup> <sub>-1400</sub>	9300 ± 1800	8.28 ± 0.34	-1.25 ± 0.84	8
19	"	IC 131	< 100	< 100	8600 ± 700	9000 <sup>+2100</sup> <sub>-1000</sub>	8.48 <sup>+0.14</sup> <sub>-0.13</sub>	-1.16 <sup>+0.32</sup> <sub>-0.36</sub>	8
20	"	IC 132	200 ± 200	< 100	10300 <sup>+400</sup> <sub>-500</sub>	10800 <sup>+1000</sup> <sub>-700</sub>	8.30 <sup>+0.07</sup> <sub>-0.06</sub>	-1.13 ± 0.16	8
21	"	NGC 588	< 100	< 100	10700 ± 400	10700 <sup>+900</sup> <sub>-700</sub>	8.23 ± 0.05	-1.28 ± 0.15	8
22	"	NGC 595	< 100	50 ± 20	7400 <sup>+300</sup> <sub>-400</sub>	8300 <sup>+200</sup> <sub>-100</sub>	8.44 <sup>+0.05</sup> <sub>-0.04</sub>	-1.04 ± 0.05	7
23	"	NGC 604	< 100	50 ± 20	8100 ± 200	8700 <sup>+300</sup> <sub>-200</sub>	8.39 ± 0.03	-0.97 ± 0.07	7
24	M81	21*	< 100	–	11200 <sup>+800</sup> <sub>-900</sub>	13300 ± 3400	8.17 ± 0.15	-0.75 ± 0.93	9
25	"	disc1*	< 100	–	6000 <sup>+1000</sup> <sub>-1200</sub>	7300 <sup>+800</sup> <sub>-900</sub>	8.88 <sup>+0.28</sup> <sub>-0.19</sub>	-0.92 <sup>+0.23</sup> <sub>-0.25</sub>	9
26	"	disc3	< 100	–	9000 <sup>+1200</sup> <sub>-1300</sub>	8300 <sup>+500</sup> <sub>-900</sub>	8.62 <sup>+0.21</sup> <sub>-0.25</sub>	-0.99 <sup>+0.32</sup> <sub>-0.36</sub>	9
27	M101	H71	< 100	100 ± 50	11300 ± 100	10400 <sup>+1400</sup> <sub>-900</sub>	8.22 ± 0.09	-1.34 <sup>+0.21</sup> <sub>-0.22</sub>	10
28	"	H98	< 100	300 ± 50	10000 ± 100	10800 <sup>+2200</sup> <sub>-1200</sub>	8.29 <sup>+0.07</sup> <sub>-0.06</sub>	-1.16 <sup>+0.27</sup> <sub>-0.29</sub>	10
29	"	H128*	100 ± 100	100 ± 40	9500 ± 100	9400 ± 300	8.36 ± 0.02	-1.09 ± 0.08	10
30	"	H140	< 100	50 ± 40	9600 ± 200	8500 <sup>+600</sup> <sub>-400</sub>	8.42 <sup>+0.09</sup> <sub>-0.10</sub>	-1.05 ± 0.14	10
31	"	H143*	< 100	–	10700 ± 600	13200 <sup>+2100</sup> <sub>-1300</sub>	8.04 ± 0.08	-0.86 <sup>+0.20</sup> <sub>-0.21</sub>	11
32	"	H143*	< 100	40 ± 30	9700 ± 100	9500 <sup>+400</sup> <sub>-300</sub>	8.33 ± 0.04	-1.1 ± 0.09	10
33	"	H149*	100 ± 100	–	9200 <sup>+900</sup> <sub>-1000</sub>	12700 <sup>+1900</sup> <sub>-1200</sub>	8.26 <sup>+0.17</sup> <sub>-0.14</sub>	-0.84 <sup>+0.20</sup> <sub>-0.21</sub>	10
34	"	H149*	100 ± 100	40 ± 30	9300 ± 100	9200 <sup>+300</sup> <sub>-200</sub>	8.44 ± 0.03	-1.1 ± 0.07	11
35	"	H185	< 100	60 ± 50	9000 <sup>+200</sup> <sub>-300</sub>	9000 <sup>+1100</sup> <sub>-700</sub>	8.37 <sup>+0.13</sup> <sub>-0.15</sub>	-0.98 <sup>+0.21</sup> <sub>-0.22</sub>	10
36	"	H206	< 100	100 ± 40	8300 <sup>+300</sup> <sub>-400</sub>	8600 <sup>+400</sup> <sub>-300</sub>	8.41 <sup>+0.07</sup> <sub>-0.08</sub>	-0.96 ± 0.11	10
37	"	H219	< 100	100 ± 40	9700 ± 200	10900 <sup>+1100</sup> <sub>-800</sub>	8.20 <sup>+0.08</sup> <sub>-0.09</sub>	-1.15 ± 0.16	10
38	"	H409	200 ± 100	–	9600 <sup>+400</sup> <sub>-500</sub>	9900 <sup>+1300</sup> <sub>-800</sub>	8.37 ± 0.08	-1.14 <sup>+0.21</sup> <sub>-0.22</sub>	10
39	"	H416*	200 ± 100	300 ± 100	9400 ± 100	9300 ± 200	8.43 ± 0.02	-1.09 ± 0.05	11
40	"	H694	< 100	100 ± 20	8400 ± 300	7900 <sup>+600</sup> <sub>-400</sub>	8.53 <sup>+0.10</sup> <sub>-0.11</sub>	-0.98 <sup>+0.15</sup> <sub>-0.16</sub>	10
41	"	H798	100 ± 50	50 ± 20	8600 ± 100	8400 <sup>+500</sup> <sub>-400</sub>	8.53 <sup>+0.05</sup> <sub>-0.06</sub>	-1.02 ± 0.12	10
42	"	H875	< 100	100 ± 40	8800 <sup>+400</sup> <sub>-500</sub>	8200 <sup>+500</sup> <sub>-400</sub>	8.43 <sup>+0.09</sup> <sub>-0.11</sub>	-0.93 ± 0.14	10
43	"	H1013*	< 100	–	6700 <sup>+400</sup> <sub>-500</sub>	8100 ± 200	8.60 <sup>+0.08</sup> <sub>-0.07</sub>	-0.88 ± 0.06	12
44	"	H1013*	< 100	100 ± 60	9000 ± 300	9500 <sup>+1000</sup> <sub>-700</sub>	8.34 <sup>+0.10</sup> <sub>-0.12</sub>	-1.11 <sup>+0.19</sup> <sub>-0.20</sub>	10
45	"	H1013*	< 100	100 ± 40	7300 <sup>+500</sup> <sub>-700</sub>	7800 ± 300	8.44 <sup>+0.11</sup> <sub>-0.08</sub>	-0.79 ± 0.10	7
46	"	H1052	100 ± 100	200 ± 040	7700 ± 100	8400 ± 200	8.58 ± 0.02	-0.97 ± 0.06	10
47	"	H1104	100 ± 50	200 ± 030	9300 ± 100	9200 <sup>+1300</sup> <sub>-800</sub>	8.37 <sup>+0.11</sup> <sub>-0.12</sub>	-1.02 <sup>+0.23</sup> <sub>-0.25</sub>	10
48	"	H1216	< 100	< 100	10700 ± 100	10100 <sup>+1600</sup> <sub>-900</sub>	8.28 <sup>+0.08</sup> <sub>-0.07</sub>	-1.31 <sup>+0.23</sup> <sub>-0.25</sub>	10
49	"	NGC 5461*	200 <sup>+200</sup> <sub>-100</sub>	200 ± 100	8500 ± 200	9100 <sup>+400</sup> <sub>-300</sub>	8.42 ± 0.04	-0.85 ± 0.09	7
50	"	NGC 5461	< 100	200 ± 40	8500 ± 100	8400 <sup>+400</sup> <sub>-300</sub>	8.50 ± 0.06	-1.03 ± 0.11	10
51	"	NGC 5461	< 100	200 ± 50	9100 ± 200	8400 <sup>+700</sup> <sub>-500</sub>	8.45 <sup>+0.10</sup> <sub>-0.11</sub>	-0.97 <sup>+0.16</sup> <sub>-0.17</sub>	10
52	"	NGC 5461	200 ± 100	200 ± 100	8700 ± 100	8800 ± 200	8.49 ± 0.02	-0.97 ± 0.05	10
53	"	NGC 5461	100 ± 2	200 ± 1	8500 ± 40	8500 ± 100	8.56 ± 0.01	-1.01 ± 0.04	13
54	"	NGC 5471	200 ± 100	200 ± 100	12700 ± 200	11100 <sup>+1000</sup> <sub>-700</sub>	8.15 ± 0.03	-1.32 ± 0.15	10
55	"	NGC 5471B*	300 ± 100	–	14000 ± 400	12300 <sup>+2100</sup> <sub>-1200</sub>	7.93 ± 0.08	-1.21 <sup>+0.22</sup> <sub>-0.23</sub>	11
56	Mrk 35	–	200 ± 30	–	10100 ± 100	11000 <sup>+600</sup> <sub>-500</sub>	8.30 ± 0.03	-1.26 ± 0.09	2
57	Mrk 1236	–	100 ± 30	–	12100 ± 100	12900 <sup>+2900</sup> <sub>-1500</sub>	8.15 <sup>+0.04</sup> <sub>-0.03</sub>	-1.2 <sup>+0.25</sup> <sub>-0.27</sub>	2
58	Mrk 1259	–	800 ± 100	–	10000 <sup>+300</sup> <sub>-400</sub>	8000 <sup>+400</sup> <sub>-300</sub>	8.40 ± 0.07	-0.79 ± 0.10	1
59	Mrk 1315	–	< 100	–	10900 ± 100	11900 <sup>+2500</sup> <sub>-1300</sub>	8.26 <sup>+0.03</sup> <sub>-0.02</sub>	-1.37 <sup>+0.26</sup> <sub>-0.27</sub>	2
60	Mrk 1329	–	< 100	–	10700 ± 100	11000 <sup>+1400</sup> <sub>-900</sub>	8.28 ± 0.03	-1.4 <sup>+0.19</sup> <sub>-0.20</sub>	2

Table A1: continued.

ID	Galaxy	H II region	$n_e$ [S II] ( $\text{cm}^{-3}$ )	$n_e$ [O II] ( $\text{cm}^{-3}$ )	$T_e$ [O III] <sup>a</sup> (K)	$T_e$ [N II] (K)	12+log(O/H)	log(N/O)	Ref.
61	Mrk 450	Mrk 450-1	100 ± 30	—	11600 ± 100	10800 <sup>+1400</sup> <sub>-900</sub>	8.20 ± 0.05	-1.35 ± 0.20	2
62	MW <sup>2</sup>	HH202	1800 <sup>+700</sup> <sub>-500</sub>	2000 <sup>+500</sup> <sub>-300</sub>	8100 ± 200	9600 <sup>+500</sup> <sub>-400</sub>	8.50 ± 0.04	-0.86 ± 0.10	14
63	"	HH202N	1500 <sup>+200</sup> <sub>-100</sub>	1900 ± 100	8200 ± 100	9400 ± 200	8.44 ± 0.02	-0.77 ± 0.05	15
64	"	HH202S	3500 <sup>+700</sup> <sub>-500</sub>	5700 <sup>+800</sup> <sub>-600</sub>	8300 <sup>+100</sup> <sub>-200</sub>	9800 ± 200	8.44 ± 0.03	-0.74 ± 0.05	15
65	"	M8	1300 ± 200	1200 <sup>+400</sup> <sub>-300</sub>	8000 ± 100	8400 ± 100	8.45 <sup>+0.02</sup> <sub>-0.03</sub>	-0.77 ± 0.04	16
66	"	M16	1100 ± 200	900 <sup>+200</sup> <sub>-100</sub>	7600 ± 200	8300 <sup>+200</sup> <sub>-100</sub>	8.54 ± 0.03	-0.70 ± 0.05	17
67	"	M17	400 ± 100	400 ± 100	7900 ± 100	8900 ± 200	8.54 ± 0.02	-0.92 ± 0.06	16
68	"	M17	500 <sup>+200</sup> <sub>-100</sub>	—	8000 ± 200	9200 <sup>+400</sup> <sub>-300</sub>	8.54 ± 0.04	-0.86 ± 0.10	4
69	"	M20	300 ± 100	200 ± 50	7700 <sup>+200</sup> <sub>-300</sub>	8300 ± 100	8.53 ± 0.03	-0.85 ± 0.05	17
70	"	M42	4700 <sup>+3400</sup> <sub>-1500</sub>	4400 <sup>+1400</sup> <sub>-900</sub>	8300 ± 40	10400 ± 200	8.51 ± 0.01	-0.77 ± 0.05	18
71	"	NGC 2579A	600 ± 200	—	9400 ± 200	11100 <sup>+600</sup> <sub>-500</sub>	8.34 ± 0.04	-0.99 ± 0.10	19
72	"	NGC 2579B	500 ± 100	—	9100 ± 200	9400 <sup>+400</sup> <sub>-300</sub>	8.45 ± 0.04	-1.04 ± 0.09	19
73	"	NGC 2579C	700 ± 100	—	8500 ± 200	11200 <sup>+700</sup> <sub>-600</sub>	8.46 ± 0.04	-0.94 ± 0.11	19
74	"	NGC 2579ABC	600 ± 100	—	8900 ± 200	10700 <sup>+300</sup> <sub>-400</sub>	8.42 ± 0.03	-0.98 ± 0.09	19
75	"	NGC 3576	1100 <sup>+400</sup> <sub>-300</sub>	1300 ± 200	8400 ± 100	8800 ± 200	8.53 ± 0.02	-0.95 ± 0.06	20
76	"	NGC 3576	1100 <sup>+300</sup> <sub>-200</sub>	1100 <sup>+300</sup> <sub>-200</sub>	8700 <sup>+200</sup> <sub>-300</sub>	9000 <sup>+400</sup> <sub>-300</sub>	8.49 ± 0.04	-0.79 <sup>+0.09</sup> <sub>-0.10</sub>	4
77	"	NGC 3603	3100 <sup>+1200</sup> <sub>-700</sub>	2000 <sup>+300</sup> <sub>-300</sub>	9000 ± 100	11300 <sup>+600</sup> <sub>-500</sub>	8.48 ± 0.03	-0.82 ± 0.09	20
78	"	NGC 7635A2	100 ± 40	—	8000 ± 500	8100 <sup>+600</sup> <sub>-400</sub>	8.46 <sup>+0.10</sup> <sub>-0.09</sub>	-0.85 <sup>+0.15</sup> <sub>-0.16</sub>	21
79	"	NGC 7635A3	100 ± 50	—	7600 <sup>+500</sup> <sub>-600</sub>	8200 <sup>+400</sup> <sub>-300</sub>	8.51 <sup>+0.12</sup> <sub>-0.09</sub>	-0.88 ± 0.12	21
80	"	NGC 7635A4	1500 <sup>+200</sup> <sub>-100</sub>	—	8700 <sup>+400</sup> <sub>-500</sub>	9100 ± 100	8.24 ± 0.03	-0.60 ± 0.03	21
81	"	S311	300 ± 100	200 ± 100	8900 ± 100	9300 ± 200	8.40 ± 0.03	-0.94 ± 0.05	22
82	"	S156	900 ± 30	—	9000 <sup>+300</sup> <sub>-400</sub>	9400 ± 400	8.33 <sup>+0.07</sup> <sub>-0.08</sub>	-0.94 ± 0.10	23
83	"	S162	1100 ± 20	—	9300 ± 200	9100 ± 300	8.36 ± 0.05	-0.94 ± 0.07	23
84	"	S212	200 ± 30	—	12000 ± 400	10700 <sup>+500</sup> <sub>-400</sub>	8.07 <sup>+0.05</sup> <sub>-0.06</sub>	-1.13 ± 0.09	23
85	"	Sh2-83	300 ± 100	—	10300 ± 400	12000 <sup>+600</sup> <sub>-500</sub>	8.29 ± 0.05	-0.81 ± 0.10	24
86	"	Sh2-100	400 <sup>+300</sup> <sub>-200</sub>	—	8200 ± 100	8600 ± 300	8.50 ± 0.03	-0.93 ± 0.09	24
87	"	Sh2-128	500 ± 100	—	10000 ± 300	10600 ± 200	8.21 <sup>+0.04</sup> <sub>-0.03</sub>	-1.00 ± 0.05	24
88	"	Sh2-288	400 <sup>+300</sup> <sub>-200</sub>	—	9200 ± 500	9400 ± 300	8.32 ± 0.06	-0.97 ± 0.09	24
89	"	Sh2-298	100 <sup>60</sup>	60 ± 30	11700 ± 200	11700 <sup>+500</sup> <sub>-400</sub>	8.42 ± 0.04	-0.80 ± 0.08	24
90	NGC 2366	NGC 2363*	100 ± 100	200 ± 100	16000 ± 300	13100 <sup>+1500</sup> <sub>-1000</sub>	7.78 ± 0.02	-1.22 ± 0.16	7
91	NGC 2403	HK 423	< 100	—	11300 ± 100	10500 <sup>+2400</sup> <sub>-1100</sub>	8.21 ± 0.10	-1.43 <sup>+0.27</sup> <sub>-0.29</sub>	25
92	"	VS 9	100 ± 100	—	11000 ± 100	9900 <sup>+600</sup> <sub>-500</sub>	8.27 ± 0.05	-1.4 ± 0.12	25
93	"	VS 24	100 ± 40	200 ± 20	8000 ± 400	8300 <sup>+400</sup> <sub>-300</sub>	8.37 ± 0.06	-0.94 <sup>+0.09</sup> <sub>-0.10</sub>	7
94	"	VS 35	< 100	—	8900 <sup>+500</sup> <sub>-600</sub>	8600 <sup>+400</sup> <sub>-300</sub>	8.42 ± 0.07	-1.07 ± 0.10	25
95	"	VS 38	< 100	—	9500 <sup>+700</sup> <sub>-800</sub>	7900 ± 300	8.48 <sup>+0.07</sup> <sub>-0.08</sub>	-1.12 ± 0.10	25
96	"	VS 38	50 ± 40	100 ± 20	8700 ± 300	8100 <sup>+500</sup> <sub>-400</sub>	8.28 ± 0.07	-0.97 ± 0.14	7
97	"	VS 44	100 ± 100	—	8600 ± 200	9000 <sup>+500</sup> <sub>-400</sub>	8.41 ± 0.05	-1.12 ± 0.11	25
98	"	VS 44	100 ± 50	100 ± 20	8200 ± 200	8900 ± 300	8.36 ± 0.04	-0.95 ± 0.08	7
99	NGC 300	2	< 100	—	11900 ± 300	12200 <sup>+1300</sup> <sub>-900</sub>	8.12 ± 0.04	-1.42 ± 0.16	26
100	"	8	< 100	—	9400 ± 400	9900 <sup>+800</sup> <sub>-600</sub>	8.24 <sup>+0.08</sup> <sub>-0.09</sub>	-1.18 ± 0.15	26
101	"	10	< 100	—	8600 ± 200	9200 <sup>+400</sup> <sub>-300</sub>	8.39 ± 0.04	-1.25 ± 0.10	26
102	"	14*	< 100	—	8700 ± 200	8600 ± 300	8.45 ± 0.05	-1.12 <sup>+0.08</sup> <sub>-0.09</sub>	26
103	"	17*	< 100	—	8100 ± 200	9300 <sup>+500</sup> <sub>-400</sub>	8.41 ± 0.05	-1.16 ± 0.12	26
104	"	19*	< 100	—	8500 ± 200	8900 <sup>+500</sup> <sub>-400</sub>	8.36 <sup>+0.05</sup> <sub>-0.06</sub>	-1.23 <sup>+0.11</sup> <sub>-0.12</sub>	26
105	"	20*	< 100	—	8100 ± 200	9100 ± 400	8.41 ± 0.04	-1.07 ± 0.11	26
106	"	23*	< 100	—	8000 <sup>+200</sup> <sub>-300</sub>	8700 <sup>+300</sup> <sub>-200</sub>	8.46 ± 0.05	-1.13 ± 0.08	26
107	"	24*	< 100	—	8300 ± 200	9100 ± 300	8.38 ± 0.04	-1.08 ± 0.09	26
108	"	26*	< 100	—	9000 ± 200	9600 <sup>+500</sup> <sub>-400</sub>	8.32 ± 0.05	-1.15 ± 0.11	26
109	"	27	< 100	—	11000 ± 300	10600 <sup>+700</sup> <sub>-500</sub>	8.16 <sup>+0.07</sup> <sub>-0.08</sub>	-1.23 ± 0.12	26
110	"	28	< 100	—	10500 ± 300	11400 <sup>+1600</sup> <sub>-1000</sub>	8.15 ± 0.09	-1.30 ± 0.21	26
111	"	R14	< 100	< 100	8200 ± 400	8300 <sup>+2100</sup> <sub>-900</sub>	8.50 <sup>+0.17</sup> <sub>-0.12</sub>	-1.17 <sup>+0.34</sup> <sub>-0.39</sub>	8
112	"	R23	< 100	< 100	7800 ± 400	8700 <sup>+1700</sup> <sub>-900</sub>	8.47 <sup>+0.12</sup> <sub>-0.13</sub>	-1.11 <sup>+0.29</sup> <sub>-0.32</sub>	8
113	NGC 3310	1	100 ± 10	—	9100 <sup>+900</sup> <sub>-1000</sub>	10100 <sup>+900</sup> <sub>-600</sub>	8.34 <sup>+0.13</sup> <sub>-0.11</sub>	-0.97 <sup>+0.15</sup> <sub>-0.16</sub>	27
114	"	4	100 ± 20	—	10200 ± 500	9300 <sup>+800</sup> <sub>-600</sub>	8.36 <sup>+0.09</sup> <sub>-0.10</sub>	-1.05 ± 0.16	27
115	"	7	100 ± 10	—	11200 <sup>+700</sup> <sub>-800</sub>	9800 <sup>+1000</sup> <sub>-700</sub>	8.18 ± 0.11	-0.89 <sup>+0.17</sup> <sub>-0.18</sub>	27
116	"	8	100 ± 20	—	10700 ± 800	9700 <sup>+600</sup> <sub>-500</sub>	8.27 ± 0.08	-0.97 ± 0.12	27
117	"	13	60 ± 10	—	10600 ± 800	11300 <sup>+500</sup> <sub>-400</sub>	8.10 <sup>+0.07</sup> <sub>-0.06</sub>	-0.87 ± 0.08	27
118	"	15	20 ± 10	—	11400 <sup>+600</sup> <sub>-700</sub>	10100 <sup>+800</sup> <sub>-600</sub>	8.20 <sup>+0.08</sup> <sub>-0.09</sub>	-0.96 <sup>+0.13</sup> <sub>-0.14</sub>	27
119	"	16	100 ± 10	—	11600 ± 700	11400 <sup>+1300</sup> <sub>-900</sub>	8.05 <sup>+0.09</sup> <sub>-0.10</sub>	-0.93 <sup>+0.17</sup> <sub>-0.17</sub>	27
120	"	21	20 ± 20	—	12700 ± 700	12100 <sup>+1400</sup> <sub>-1000</sub>	7.96 <sup>+0.10</sup> <sub>-0.11</sub>	-0.91 <sup>+0.19</sup> <sub>-0.18</sub>	27
121	NGC 5253	C1	500 ± 50	—	12200 ± 100	11400 ± 100	8.16 ± 0.01	-0.82 <sup>+0.02</sup> <sub>-0.03</sub>	1
122	"	C2	200 ± 30	—	10200 ± 100	11000 ± 400	8.27 ± 0.01	-1.23 ± 0.07	1

Table A1: continued.

ID	Galaxy	H II region	$n_e$ [S II] ( $\text{cm}^{-3}$ )	$n_e$ [O II] ( $\text{cm}^{-3}$ )	$T_e$ [O III] <sup>a</sup> (K)	$T_e$ [N II] (K)	12+log(O/H)	log(N/O)	Ref.
123	"	HIII*	400 ± 100	300 ± 100	11900 ± 200	10800 <sup>+600</sup> <sub>-500</sub>	8.21 ± 0.03	-0.93 ± 0.10	28
124	"	HII2*	400 ± 100	300 ± 100	11800 ± 200	10700 <sup>+700</sup> <sub>-500</sub>	8.21 ± 0.03	-0.88 ± 0.11	28
125	"	P2	800 ± 100	-	12300 ± 100	11200 ± 200	8.17 ± 0.01	-0.78 <sup>+0.03</sup> <sub>-0.04</sub>	1
126	"	UV1*	300 ± 100	100±	10800 ± 200	10000 <sup>+800</sup> <sub>-600</sub>	8.29 <sup>+0.05</sup> <sub>-0.04</sub>	-1.42 ± 0.15	28
127	"	NGC 5408	200 ± 100	200 ± 100	15500 ± 400	11800 <sup>+1000</sup> <sub>-700</sub>	7.87 ± 0.03	-1.55 ± 0.14	29
128	NGC 628	+31.6-191.1	50 ± 20	200 ± 50	8400 <sup>+400</sup> <sub>-500</sub>	8500 <sup>+700</sup> <sub>-500</sub>	8.44 <sup>+0.09</sup> <sub>-0.11</sub>	-1.00 <sup>+0.16</sup> <sub>-0.17</sub>	30
129	"	-42.8-158.2	100 ± 30	< 100	8300 ± 400	8200 <sup>+800</sup> <sub>-600</sub>	8.45 <sup>+0.11</sup> <sub>-0.12</sub>	-0.99 ± 0.20	30
130	"	-90+186	50 ± 30	-	9400 ± 500	8800 ± 200	8.39 ± 0.05	-1.05 ± 0.06	25
131	"	-90.1+190.20	100 ± 30	300 ± 40	8800 ± 400	8500 <sup>+700</sup> <sub>-500</sub>	8.47 <sup>+0.10</sup> <sub>-0.11</sub>	-1.09 ± 0.16	30
132	"	+131.9+18.5	300 ± 40	200 ± 30	10800 <sup>+400</sup> <sub>-500</sub>	7800 <sup>+500</sup> <sub>-400</sub>	8.43 <sup>+0.10</sup> <sub>-0.11</sub>	-0.85 ± 0.13	30
133	"	+151.0+22.3	100 ± 30	< 100	9200 <sup>+600</sup> <sub>-700</sub>	7900 <sup>+600</sup> <sub>-400</sub>	8.44 <sup>+0.10</sup> <sub>-0.11</sub>	-0.86 ± 0.16	30
134	"	-184.7+83.4	100 ± 30	100 ± 20	9400 ± 400	8000 <sup>+600</sup> <sub>-400</sub>	8.53 <sup>+0.11</sup> <sub>-0.13</sub>	-1.06 ± 0.16	30
135	"	-190+180	100 ± 50	-	9200 ± 500	8400 ± 200	8.44 ± 0.04	-1.03 ± 0.06	25
136	"	-200.6-4.2	< 100	< 100	9000 ± 400	9100 <sup>+1600</sup> <sub>-900</sub>	8.30 <sup>+0.15</sup> <sub>-0.17</sub>	-0.96 <sup>+0.26</sup> <sub>-0.29</sub>	30
137	"	+252.1-92.1	< 100	< 100	11900 ± 800	12000 <sup>+1900</sup> <sub>-1200</sub>	7.97 ± 0.10	-0.96 <sup>+0.21</sup> <sub>-0.23</sub>	30
138	NGC 6822	V	100 ± 30	-	11300 ± 100	11900 <sup>+600</sup> <sub>-500</sub>	8.16 ± 0.01	-1.35 ± 0.09	1
139	"	HV	< 100	100 ± 100	11500 ± 200	11500 <sup>+1100</sup> <sub>-1100</sub>	8.17 ± 0.04	-1.45 <sup>+0.23</sup> <sub>-0.24</sub>	29
140	SHOC 011 <sup>3</sup>	(SDSS) <sup>6*</sup>	100 ± 100	-	11200 ± 200	12800 <sup>+1300</sup> <sub>-900</sub>	8.14 ± 0.03	-0.94 ± 0.15	31
141	"	(WHT) <sup>7*</sup>	100 ± 100	-	12500 ± 300	11100 <sup>+1200</sup> <sub>-800</sub>	8.06 ± 0.05	-0.95 ± 0.17	31
142	SHOC 575 <sup>4*</sup>	-	100 ± 50	-	12500 ± 200	13200 <sup>+800</sup> <sub>-600</sub>	8.05 ± 0.02	-0.95 ± 0.09	32
143	SMC <sup>5</sup>	N66	< 100	< 100	12600 ± 500	12800 <sup>+800</sup> <sub>-600</sub>	8.02 ± 0.05	-1.45 ± 0.10	4
144	"	N66A	200 ± 100	100 ± 100	12500 ± 200	12200 <sup>+500</sup> <sub>-400</sub>	8.00 ± 0.02	-1.5 ± 0.07	5
145	"	N81	300 ± 100	400 <sup>+200</sup> <sub>-100</sub>	12700 ± 200	11800 <sup>+400</sup> <sub>-300</sub>	8.03 ± 0.02	-1.59 ± 0.07	5
146	"	N88A	2200 <sup>+2400</sup> <sub>-900</sub>	2000 <sup>+2100</sup> <sub>-800</sub>	14900 ± 500	13400 <sup>+1500</sup> <sub>-1100</sub>	7.91 ± 0.04	-1.43 ± 0.17	5
147	"	NGC 456 No.1	300 ± 30	-	12200 ± 100	11900 ± 300	8.05 ± 0.02	-1.58 ± 0.05	1
148	"	NGC 456 No.2	100 ± 30	-	11900 ± 100	10900 <sup>+1300</sup> <sub>-900</sub>	8.08 <sup>+0.05</sup> <sub>-0.04</sub>	-1.59 <sup>+0.18</sup> <sub>-0.19</sub>	1
149	"	NGC 456 No.3	100 ± 30	-	12000 ± 100	12100 <sup>+1200</sup> <sub>-800</sub>	8.03 ± 0.03	-1.61 ± 0.15	1
150	"	NGC 456 No.1	100 ± 100	100 ± 20	12500 ± 300	10700 <sup>+1900</sup> <sub>-1100</sub>	8.02 ± 0.10	-1.34 <sup>+0.25</sup> <sub>-0.26</sub>	33
151	"	NGC 456 No.2	200 ± 100	200 ± 10	12000 ± 200	11200 <sup>+1300</sup> <sub>-900</sub>	8.06 ± 0.05	-1.49 <sup>+0.18</sup> <sub>-0.19</sub>	33
152	TOL 89	No.1	100 ± 30	-	10200 ± 100	10700 ± 400	8.32 ± 0.02	-1.23 <sup>+0.08</sup> <sub>-0.07</sub>	1
153	TOL 1457-262	-	100 ± 30	-	11800 ± 100	9300 <sup>+400</sup> <sub>-300</sub>	8.41 ± 0.04	-1.78 ± 0.09	1
154	TOL 2138-405	No.1	300 ± 30	-	13800 ± 100	11800 <sup>+1300</sup> <sub>-900</sub>	8.05 ± 0.03	-1.15 <sup>+0.16</sup> <sub>-0.17</sub>	1

References for the line intensities: (1) Guseva et al. (2011), (2) Izotov & Thuan (2004), (3) Peimbert (2003), (4) Tsamis et al. (2003), (5) Toribio San Cipriano et al. (2017), (6) Zurita & Bresolin (2012), (7) Esteban et al. (2009), (8) Toribio San Cipriano et al. (2016), (9) Patterson et al. (2012), (10) Croxall et al. (2016), (11) Kennicutt et al. (2003), (12) Bresolin (2007), (13) Luridiana et al. (2002), (14) Mesa-Delgado et al. (2009), (15) Espíritu et al. (2017), (16) García-Rojas et al. (2007), (17) García-Rojas et al. (2006), (18) Esteban et al. (2004), (19) Copetti et al. (2007), (20) García-Rojas et al. (2004), (21) Esteban et al. (2016), (22) García-Rojas et al. (2005), (23) Fernández-Martín et al. (2017), (24) Esteban et al. (2017), (25) Berg et al. (2013), (26) Bresolin et al. (2009), (27) Miralles-Caballero et al. (2014), (28) López-Sánchez et al. (2007), (29) Esteban et al. (2014), (30) Berg et al. (2015), (31) Hägele et al. (2006), (32) Hägele et al. (2008), (33) Peña-Guerrero et al. (2012). <sup>a</sup>The objects with  $T_e$ [O III] < 10000 K and low-resolution spectra have been corrected using Equation 2 (see section 3.2). <sup>1</sup>Large Magellanic Cloud. <sup>2</sup>The Milky Way. <sup>3</sup>SDSS J002101.03+005248.1 is the object ID used in the original study. <sup>4</sup>SDSS J172906.56+565319.4 is the object ID used in the original study. <sup>5</sup>Small Magellanic Cloud. <sup>6</sup>Spectrum from the Sloan Digital Sky Survey (SDSS). <sup>7</sup>Spectrum from the William Herschel Telescope. \*H II regions with Wolf-Rayet features.

Table A2: Our calculated values for the oxygen abundances using  $T_e$  and the R, S, ONS, C, O3N2, and N2 strong-line methods for the sample of extragalactic H II regions.

ID	Galaxy	Region	$T_e$	R	S	12+log(O/H)			
						ONS	C	O3N2	N2
1	He 2-10	C	$8.46^{+0.03}_{-0.04}$	$8.60\pm 0.10$	$8.59\pm 0.10$	$8.49\pm 0.10$	$8.50\pm 0.10$	$8.39\pm 0.18$	$8.52\pm 0.16$
2	HS 0924+3821	–	$8.04\pm 0.04$	$8.18\pm 0.10$	$8.18\pm 0.10$	$8.17\pm 0.10$	$8.11\pm 0.10$	–	$8.14\pm 0.16$
3	HS 1213+3636A	–	$8.13^{+0.09}_{-0.08}$	$8.09\pm 0.10$	$8.08\pm 0.10$	$8.22\pm 0.10$	$8.23\pm 0.10$	$8.17\pm 0.18$	$8.18\pm 0.16$
4	J1253–0312	–	$8.03\pm 0.01$	$8.33\pm 0.10$	$8.34\pm 0.10$	$8.41\pm 0.10$	$8.29\pm 0.10$	–	$8.13\pm 0.16$
5	LMC	30 Doradus	$8.36\pm 0.01$	$8.13\pm 0.10$	$8.16\pm 0.10$	$8.25\pm 0.10$	$8.25\pm 0.10$	–	$8.10\pm 0.16$
6	"	30 Doradus	$8.30\pm 0.05$	$8.07\pm 0.10$	$8.09\pm 0.10$	$8.21\pm 0.10$	$8.23\pm 0.10$	–	$8.03\pm 0.16$
7	"	IC 2111	$8.43\pm 0.03$	$8.18\pm 0.10$	$8.29\pm 0.10$	$8.31\pm 0.10$	$8.32\pm 0.10$	$8.19\pm 0.18$	$8.23\pm 0.16$
8	"	N11B	$8.40\pm 0.05$	$8.07\pm 0.10$	$8.07\pm 0.10$	$8.23\pm 0.10$	$8.22\pm 0.10$	–	$8.15\pm 0.16$
9	"	N11B	$8.39\pm 0.02$	$8.21\pm 0.10$	$8.28\pm 0.10$	$8.29\pm 0.10$	$8.29\pm 0.10$	$8.18\pm 0.18$	$8.21\pm 0.16$
10	"	N44C	$8.28\pm 0.03$	$8.14\pm 0.10$	$8.10\pm 0.10$	$8.15\pm 0.10$	$8.06\pm 0.10$	–	–
11	"	NGC 1714	$8.36\pm 0.03$	$8.01\pm 0.10$	$8.05\pm 0.10$	$8.20\pm 0.10$	$8.25\pm 0.10$	–	$8.06\pm 0.16$
12	M31	17	$8.46\pm 0.08$	$8.53\pm 0.10$	$8.53\pm 0.10$	$8.55\pm 0.10$	$8.50\pm 0.10$	$8.38\pm 0.18$	$8.44\pm 0.16$
13	"	25	$8.32\pm 0.05$	$8.39\pm 0.10$	$8.40\pm 0.10$	$8.46\pm 0.10$	$8.42\pm 0.10$	$8.24\pm 0.18$	$8.30\pm 0.16$
14	"	26	$8.32^{+0.07}_{-0.06}$	$8.43\pm 0.10$	$8.44\pm 0.10$	$8.52\pm 0.10$	$8.42\pm 0.10$	$8.30\pm 0.18$	$8.39\pm 0.16$
15	"	35	$8.43\pm 0.06$	$8.41\pm 0.10$	$8.39\pm 0.10$	$8.47\pm 0.10$	$8.37\pm 0.10$	$8.22\pm 0.18$	$8.31\pm 0.16$
16	"	K932	$8.44\pm 0.03$	$8.40\pm 0.10$	$8.41\pm 0.10$	$8.49\pm 0.10$	$8.43\pm 0.10$	$8.23\pm 0.18$	$8.30\pm 0.16$
17	M33	BCLMP 290	$8.44^{+0.13}_{-0.10}$	$8.30\pm 0.10$	$8.34\pm 0.10$	$8.35\pm 0.10$	$8.36\pm 0.10$	$8.26\pm 0.18$	$8.27\pm 0.16$
18	"	BCLMP 626	$8.28\pm 0.34$	$8.24\pm 0.10$	$8.26\pm 0.10$	$8.27\pm 0.10$	$8.29\pm 0.10$	$8.26\pm 0.18$	$8.26\pm 0.16$
19	"	IC 131	$8.48^{+0.14}_{-0.13}$	$8.31\pm 0.10$	$8.24\pm 0.10$	$8.27\pm 0.10$	$8.20\pm 0.10$	$8.20\pm 0.18$	$8.25\pm 0.16$
20	"	IC 132	$8.30^{+0.07}_{-0.06}$	$8.08\pm 0.10$	$8.04\pm 0.10$	$8.18\pm 0.10$	$8.05\pm 0.10$	$8.02\pm 0.18$	–
21	"	NGC 588	$8.23\pm 0.05$	$8.03\pm 0.10$	$8.02\pm 0.10$	$8.12\pm 0.10$	$8.00\pm 0.10$	$8.06\pm 0.18$	$8.03\pm 0.16$
22	"	NGC 595	$8.44^{+0.05}_{-0.04}$	$8.39\pm 0.10$	$8.49\pm 0.10$	$8.52\pm 0.10$	$8.51\pm 0.10$	$8.37\pm 0.18$	$8.37\pm 0.16$
23	"	NGC 604	$8.39\pm 0.03$	$8.40\pm 0.10$	$8.34\pm 0.10$	$8.36\pm 0.10$	$8.33\pm 0.10$	$8.25\pm 0.18$	$8.27\pm 0.16$
24	M81	21*	$8.17\pm 0.15$	$8.43\pm 0.10$	$8.38\pm 0.10$	$8.48\pm 0.10$	$8.33\pm 0.10$	$8.20\pm 0.18$	$8.34\pm 0.16$
25	"	disc1*	$8.88^{+0.28}_{-0.19}$	$8.61\pm 0.10$	$8.60\pm 0.10$	$8.45\pm 0.10$	$8.49\pm 0.10$	$8.47\pm 0.18$	$8.56\pm 0.16$
26	"	disc3	$8.62^{+0.21}_{-0.25}$	$8.54\pm 0.10$	$8.53\pm 0.10$	$8.42\pm 0.10$	$8.43\pm 0.10$	$8.32\pm 0.18$	$8.48\pm 0.16$
27	M101	H71	$8.22\pm 0.09$	$8.17\pm 0.10$	$8.21\pm 0.10$	$8.23\pm 0.10$	$8.19\pm 0.10$	$8.16\pm 0.18$	$8.21\pm 0.16$
28	"	H98	$8.29^{+0.07}_{-0.06}$	$8.26\pm 0.10$	$8.25\pm 0.10$	$8.29\pm 0.10$	$8.25\pm 0.10$	$8.16\pm 0.18$	$8.21\pm 0.16$
29	"	H128*	$8.36\pm 0.02$	$8.33\pm 0.10$	$8.30\pm 0.10$	$8.35\pm 0.10$	$8.28\pm 0.10$	$8.17\pm 0.18$	$8.23\pm 0.16$
30	"	H140	$8.42^{+0.09}_{-0.10}$	$8.43\pm 0.10$	$8.39\pm 0.10$	$8.44\pm 0.10$	$8.34\pm 0.10$	$8.36\pm 0.18$	$8.42\pm 0.16$
31	"	H143*	$8.04\pm 0.08$	$8.35\pm 0.10$	$8.32\pm 0.10$	$8.37\pm 0.10$	$8.29\pm 0.10$	$8.24\pm 0.18$	$8.31\pm 0.16$
32	"	H143*	$8.33\pm 0.04$	$8.35\pm 0.10$	$8.33\pm 0.10$	$8.38\pm 0.10$	$8.28\pm 0.10$	$8.25\pm 0.18$	$8.33\pm 0.16$
33	"	H149*	$8.26^{+0.17}_{-0.14}$	$8.38\pm 0.10$	$8.35\pm 0.10$	$8.41\pm 0.10$	$8.30\pm 0.10$	$8.23\pm 0.18$	$8.33\pm 0.16$
34	"	H149*	$8.44\pm 0.03$	$8.36\pm 0.10$	$8.34\pm 0.10$	$8.40\pm 0.10$	$8.30\pm 0.10$	$8.23\pm 0.18$	$8.32\pm 0.16$
35	"	H185	$8.37^{+0.13}_{-0.15}$	$8.44\pm 0.10$	$8.44\pm 0.10$	$8.45\pm 0.10$	$8.38\pm 0.10$	$8.38\pm 0.18$	$8.44\pm 0.16$
36	"	H206	$8.41^{+0.07}_{-0.08}$	$8.46\pm 0.10$	$8.45\pm 0.10$	$8.47\pm 0.10$	$8.44\pm 0.10$	$8.41\pm 0.18$	$8.46\pm 0.16$
37	"	H219	$8.20^{+0.08}_{-0.09}$	$8.27\pm 0.10$	$8.35\pm 0.10$	$8.40\pm 0.10$	$8.35\pm 0.10$	$8.32\pm 0.18$	$8.36\pm 0.16$
38	"	H409	$8.37\pm 0.08$	$8.31\pm 0.10$	$8.31\pm 0.10$	$8.35\pm 0.10$	$8.28\pm 0.10$	$8.19\pm 0.18$	$8.27\pm 0.16$
39	"	H416*	$8.43\pm 0.02$	$8.36\pm 0.10$	$8.34\pm 0.10$	$8.41\pm 0.10$	$8.29\pm 0.10$	$8.19\pm 0.18$	$8.28\pm 0.16$
40	"	H694	$8.53^{+0.10}_{-0.11}$	$8.48\pm 0.10$	$8.50\pm 0.10$	$8.48\pm 0.10$	$8.45\pm 0.10$	$8.38\pm 0.18$	$8.45\pm 0.16$
41	"	H798	$8.53^{+0.05}_{-0.06}$	$8.44\pm 0.10$	$8.43\pm 0.10$	$8.51\pm 0.10$	$8.39\pm 0.10$	$8.28\pm 0.18$	$8.38\pm 0.16$
42	"	H875	$8.43^{+0.09}_{-0.11}$	$8.49\pm 0.10$	$8.46\pm 0.10$	$8.48\pm 0.10$	$8.42\pm 0.10$	$8.42\pm 0.18$	$8.46\pm 0.16$
43	"	H1013*	$8.60^{+0.08}_{-0.07}$	$8.51\pm 0.10$	$8.55\pm 0.10$	$8.49\pm 0.10$	$8.52\pm 0.10$	$8.40\pm 0.18$	$8.46\pm 0.16$
44	"	H1013*	$8.34^{+0.07}_{-0.10}$	$8.35\pm 0.10$	$8.41\pm 0.10$	$8.46\pm 0.10$	$8.41\pm 0.10$	$8.33\pm 0.18$	$8.39\pm 0.16$
45	"	H1013*	$8.44^{+0.11}_{-0.08}$	$8.52\pm 0.10$	$8.53\pm 0.10$	$8.58\pm 0.10$	$8.50\pm 0.10$	$8.39\pm 0.18$	$8.43\pm 0.16$
46	"	H1052	$8.58\pm 0.02$	$8.44\pm 0.10$	$8.43\pm 0.10$	$8.52\pm 0.10$	$8.43\pm 0.10$	$8.26\pm 0.18$	$8.35\pm 0.16$
47	"	H1104	$8.37^{+0.11}_{-0.12}$	$8.41\pm 0.10$	$8.37\pm 0.10$	$8.42\pm 0.10$	$8.32\pm 0.10$	$8.29\pm 0.18$	$8.38\pm 0.16$
48	"	H1216	$8.28^{+0.08}_{-0.07}$	$8.15\pm 0.10$	$8.15\pm 0.10$	$8.22\pm 0.10$	$8.17\pm 0.10$	–	$8.16\pm 0.16$
49	"	NGC 5461*	$8.42\pm 0.04$	$8.34\pm 0.10$	$8.37\pm 0.10$	$8.44\pm 0.10$	$8.34\pm 0.10$	$8.22\pm 0.18$	$8.29\pm 0.16$
50	"	NGC 5461	$8.50\pm 0.06$	$8.44\pm 0.10$	$8.37\pm 0.10$	$8.50\pm 0.10$	$8.39\pm 0.10$	$8.32\pm 0.18$	$8.40\pm 0.16$
51	"	NGC 5461	$8.45^{+0.10}_{-0.11}$	$8.44\pm 0.10$	$8.44\pm 0.10$	$8.48\pm 0.10$	$8.36\pm 0.10$	$8.35\pm 0.18$	$8.43\pm 0.16$
52	"	NGC 5461	$8.49\pm 0.02$	$8.47\pm 0.10$	$8.43\pm 0.10$	$8.48\pm 0.10$	$8.35\pm 0.10$	$8.24\pm 0.18$	$8.37\pm 0.16$
53	"	NGC 5461	$8.56\pm 0.01$	$8.43\pm 0.10$	$8.39\pm 0.10$	$8.47\pm 0.10$	$8.33\pm 0.10$	$8.24\pm 0.18$	$8.35\pm 0.16$
54	"	NGC 5471	$8.15\pm 0.03$	$8.15\pm 0.10$	$8.15\pm 0.10$	$8.14\pm 0.10$	$8.09\pm 0.10$	–	$8.04\pm 0.16$
55	"	NGC 5471B*	$7.93\pm 0.08$	$8.13\pm 0.10$	$8.14\pm 0.10$	$8.06\pm 0.10$	$7.99\pm 0.10$	–	$8.17\pm 0.16$
56	Mrk 35	–	$8.30\pm 0.03$	$8.20\pm 0.10$	$8.25\pm 0.10$	$8.28\pm 0.10$	$8.24\pm 0.10$	$8.15\pm 0.18$	$8.20\pm 0.16$
57	Mrk 1236	–	$8.15^{+0.04}_{-0.03}$	$8.17\pm 0.10$	$8.17\pm 0.10$	$8.02\pm 0.10$	$8.09\pm 0.10$	–	$8.07\pm 0.16$
58	Mrk 1259	–	$8.40\pm 0.07$	$8.58\pm 0.10$	$8.56\pm 0.10$	$8.52\pm 0.10$	$8.50\pm 0.10$	$8.37\pm 0.18$	$8.50\pm 0.16$
59	Mrk 1315	–	$8.26^{+0.03}_{-0.02}$	$8.01\pm 0.10$	$8.03\pm 0.10$	$8.09\pm 0.10$	$8.06\pm 0.10$	–	–
60	Mrk 1329	–	$8.28\pm 0.03$	$8.02\pm 0.10$	$8.03\pm 0.10$	$8.10\pm 0.10$	$8.10\pm 0.10$	–	–
61	Mrk 450	Mrk 450–1	$8.20\pm 0.05$	$8.12\pm 0.10$	$8.13\pm 0.10$	$8.14\pm 0.10$	$8.11\pm 0.10$	–	$8.09\pm 0.16$

Table A2: (continued)

ID	Galaxy	Region	T <sub>e</sub>	R	S	12+log(O/H)			
						ONS	C	O3N2	N2
90	NGC 2366	NGC 2363*	7.78 ± 0.02	7.88±0.10	7.73±0.10	7.85±0.10	7.78 ±0.10	–	–
91	NGC 2403	HK 423	8.21 ± 0.10	8.07±0.10	8.07±0.10	8.18±0.10	8.18 ±0.10	–	8.12±0.16
92	"	VS 9	8.27 ± 0.05	8.12±0.10	8.12±0.10	8.20±0.10	8.19 ±0.10	8.15±0.18	8.19±0.16
93	"	VS 24	8.37 ± 0.06	8.44±0.10	8.43±0.10	8.47±0.10	8.42 ±0.10	8.32±0.18	8.35±0.16
94	"	VS 35	8.42 ± 0.07	8.40±0.10	8.45±0.10	8.50±0.10	8.42 ±0.10	8.35±0.18	8.40±0.16
95	"	VS 38	8.48 <sup>+0.07</sup> <sub>-0.08</sub>	8.39±0.10	8.42±0.10	8.46±0.10	8.40 ±0.10	8.34±0.18	8.37±0.16
96	"	VS 38	8.28 ± 0.07	8.41±0.10	8.40±0.10	8.40±0.10	8.40 ±0.10	8.28±0.18	8.28±0.16
97	"	VS 44	8.41 ± 0.05	8.34±0.10	8.37±0.10	8.41±0.10	8.36 ±0.10	8.28±0.18	8.33±0.16
98	"	VS 44	8.36 ± 0.04	8.40±0.10	8.36±0.10	8.38±0.10	8.34 ±0.10	8.27±0.18	8.30±0.16
99	NGC 300	2	8.12 ± 0.04	8.00±0.10	7.99±0.10	7.96±0.10	7.92 ±0.10	–	8.02±0.16
100	"	8	8.24 <sup>+0.08</sup> <sub>-0.09</sub>	8.27±0.10	8.36±0.10	8.39±0.10	8.37 ±0.10	8.30±0.18	8.32±0.16
101	"	10	8.39 ± 0.04	8.25±0.10	8.22±0.10	8.21±0.10	8.20 ±0.10	8.20±0.18	8.20±0.16
102	"	14*	8.45 ± 0.05	8.37±0.10	8.40±0.10	8.45±0.10	8.38 ±0.10	8.30±0.18	8.35±0.16
103	"	17*	8.41 ± 0.05	8.29±0.10	8.30±0.10	8.32±0.10	8.30 ±0.10	8.25±0.18	8.27±0.16
104	"	19*	8.36 <sup>+0.05</sup> <sub>-0.06</sub>	8.27±0.10	8.27±0.10	8.26±0.10	8.29 ±0.10	8.25±0.18	8.24±0.16
105	"	20*	8.41 ± 0.04	8.34±0.10	8.27±0.10	8.28±0.10	8.27 ±0.10	8.23±0.18	8.24±0.16
106	"	23*	8.46 ± 0.05	8.33±0.10	8.31±0.10	8.32±0.10	8.31 ±0.10	8.25±0.18	8.28±0.16
107	"	24*	8.38 ± 0.04	8.35±0.10	8.34±0.10	8.37±0.10	8.34 ±0.10	8.28±0.18	8.31±0.16
108	"	26*	8.32 ± 0.05	8.29±0.10	8.23±0.10	8.23±0.10	8.23 ±0.10	8.20±0.18	8.21±0.16
109	"	27	8.16 <sup>+0.07</sup> <sub>-0.08</sub>	8.22±0.10	8.34±0.10	8.37±0.10	8.36 ±0.10	8.28±0.18	8.30±0.16
110	"	28	8.15 ± 0.09	8.15±0.10	8.24±0.10	8.25±0.10	8.25 ±0.10	8.21±0.18	8.22±0.16
111	"	R14	8.50 <sup>+0.17</sup> <sub>-0.21</sub>	8.35±0.10	8.35±0.10	8.38±0.10	8.34 ±0.10	8.28±0.18	8.32±0.16
112	"	R23	8.47 <sup>+0.13</sup> <sub>-0.11</sub>	8.35±0.10	8.33±0.10	8.35±0.10	8.33 ±0.10	8.26±0.18	8.28±0.16
113	NGC 3310	1	8.34 <sup>+0.13</sup> <sub>-0.10</sub>	8.41±0.10	8.38±0.10	8.44±0.10	8.33 ±0.10	8.28±0.18	8.39±0.16
114	"	4	8.36 <sup>+0.09</sup> <sub>-0.10</sub>	8.41±0.10	8.38±0.10	8.44±0.10	8.29 ±0.10	8.30±0.18	8.40±0.16
115	"	7	8.18 ± 0.11	8.47±0.10	8.43±0.10	8.46±0.10	8.34 ±0.10	8.34±0.18	8.44±0.16
116	"	8	8.27 ± 0.08	8.44±0.10	8.40±0.10	8.46±0.10	8.30 ±0.10	8.31±0.18	8.42±0.16
117	"	13	8.10 <sup>+0.07</sup> <sub>-0.06</sub>	8.44±0.10	8.39±0.10	8.44±0.10	8.29 ±0.10	8.33±0.18	8.43±0.16
118	"	15	8.20 <sup>+0.08</sup> <sub>-0.09</sub>	8.43±0.10	8.38±0.10	8.43±0.10	8.27 ±0.10	8.32±0.18	8.42±0.16
119	"	16	8.05 <sup>+0.09</sup> <sub>-0.10</sub>	8.40±0.10	8.36±0.10	8.42±0.10	8.27 ±0.10	8.32±0.18	8.41±0.16
120	"	21	7.96 <sup>+0.10</sup> <sub>-0.11</sub>	8.40±0.10	8.35±0.10	8.40±0.10	8.26 ±0.10	8.32±0.18	8.41±0.16
121	NGC 5253	C1	8.16 ± 0.01	8.40±0.10	8.31±0.10	8.47±0.10	8.32 ±0.10	–	8.22±0.16
122	"	C2	8.27 ± 0.01	8.11±0.10	8.11±0.10	8.16±0.10	8.08 ±0.10	–	8.11±0.16
123	"	HII1*	8.21 ± 0.03	8.37±0.10	8.30±0.10	8.43±0.10	8.29 ±0.10	–	8.25±0.16
124	"	HII2*	8.21 ± 0.03	8.40±0.10	8.32±0.10	8.45±0.10	8.29 ±0.10	8.16±0.18	8.29±0.16
125	"	P2	8.17 ± 0.01	8.43±0.10	8.35±0.10	8.56±0.10	8.38 ±0.10	–	8.28±0.16
126	"	UV1*	8.29 <sup>+0.05</sup> <sub>-0.04</sub>	8.09±0.10	8.10±0.10	8.14±0.10	8.14 ±0.10	–	8.10±0.16
127	"	NGC 5408	7.87 ± 0.03	7.83±0.10	7.82±0.10	7.78±0.10	7.78 ±0.10	–	–
128	NGC 628	+31.6–191.1	8.44 <sup>+0.09</sup> <sub>-0.10</sub>	8.44±0.10	8.45±0.10	8.50±0.10	8.41 ±0.10	8.34±0.18	8.40±0.16
129	"	–42.8–158.2	8.45 <sup>+0.10</sup> <sub>-0.12</sub>	8.44±0.10	8.44±0.10	8.49±0.10	8.41 ±0.10	8.33±0.18	8.38±0.16
130	"	–90+186	8.39 ± 0.05	8.41±0.10	8.44±0.10	8.50±0.10	8.42 ±0.10	8.33±0.18	8.40±0.16
131	"	–90.1+190.2	8.47 <sup>+0.10</sup> <sub>-0.10</sub>	8.41±0.10	8.45±0.10	8.50±0.10	8.43 ±0.10	8.34±0.18	8.40±0.16
132	"	+131.9+18.5	8.43 <sup>+0.10</sup> <sub>-0.11</sub>	8.55±0.10	8.52±0.10	8.50±0.10	8.44 ±0.10	8.42±0.18	8.49±0.16
133	"	+151.0+22.3	8.44 <sup>+0.10</sup> <sub>-0.11</sub>	8.53±0.10	8.51±0.10	8.52±0.10	8.47 ±0.10	8.35±0.18	8.45±0.16
134	"	–184.7+83.4	8.53 <sup>+0.11</sup> <sub>-0.13</sub>	8.45±0.10	8.44±0.10	8.46±0.10	8.38 ±0.10	8.36±0.18	8.42±0.16
135	"	–190+180	8.44 ± 0.04	8.44±0.10	8.43±0.10	8.48±0.10	8.38 ±0.10	8.37±0.18	8.42±0.16
136	"	–200.6–4.2	8.30 <sup>+0.15</sup> <sub>-0.17</sub>	8.43±0.10	8.44±0.10	8.49±0.10	8.40 ±0.10	8.34±0.18	8.39±0.16
137	"	+252.1–92.1	7.97 ± 0.10	8.33±0.10	8.35±0.10	8.39±0.10	8.34 ±0.10	8.26±0.18	8.32±0.16
138	NGC 6822	V	8.16 ± 0.01	7.91±0.10	7.92±0.10	8.04±0.10	8.00 ±0.10	–	–
139	"	HV	8.17 ± 0.04	7.94±0.10	7.95±0.10	7.81±0.10	8.06 ±0.10	–	–
140	SHOC 011	(SDSS)*	8.14 ± 0.03	8.31±0.10	8.28±0.10	8.34±0.10	8.26 ±0.10	8.16±0.18	8.24±0.16
141	"	(WHT)*	8.06 ± 0.05	8.35±0.10	8.32±0.10	8.39±0.10	8.30 ±0.10	8.17±0.18	8.26±0.16
142	SHOC 575	–	8.05 ± 0.02	8.30±0.10	8.29±0.10	8.36±0.10	8.28 ±0.10	–	8.23±0.16
143	SMC	N66	8.02 ± 0.05	7.88±0.10	7.90±0.10	7.76±0.10	7.79 ±0.10	–	–
144	"	N66A	8.00 ± 0.02	7.88±0.10	7.89±0.10	7.76±0.10	8.07 ±0.10	–	–
145	"	N81	8.03 ± 0.02	7.80±0.10	7.86±0.10	7.99±0.10	8.12 ±0.10	–	–
146	"	N88A	7.91 ± 0.04	7.91±0.10	7.94±0.10	8.08±0.10	8.13 ±0.10	–	–
147	"	NGC 456 No.1	8.05 ± 0.02	7.90±0.10	7.91±0.10	8.06±0.10	8.21 ±0.10	–	8.03±0.16
148	"	NGC 456 No.2	8.08 <sup>+0.05</sup> <sub>-0.04</sub>	7.81±0.10	7.83±0.10	7.69±0.10	7.72 ±0.10	–	–
149	"	NGC 456 No.3	8.03 ± 0.03	7.79±0.10	7.82±0.10	7.99±0.10	8.07 ±0.10	–	–
150	"	NGC 456 No.1	8.02 ± 0.10	7.97±0.10	7.98±0.10	8.16±0.10	8.15 ±0.10	–	8.08±0.16
151	"	NGC 456 No.2	8.06 ± 0.05	7.89±0.10	7.90±0.10	8.06±0.10	8.02 ±0.10	–	–
152	TOL 89	No.1	8.32 ± 0.02	8.15±0.10	8.16±0.10	8.22±0.10	8.19 ±0.10	–	8.13±0.16
153	TOL 1457–262	–	8.41 ± 0.04	8.09±0.10	8.11±0.10	7.98±0.10	8.11 ±0.10	–	8.03±0.16

Table A2: (continued)

ID	Galaxy	Region	$T_e$	R	S	$12+\log(\text{O}/\text{H})$		O3N2	N2
						ONS	C		
154	TOL 2138-405	No.1	$8.05 \pm 0.03$	$8.25 \pm 0.10$	$8.25 \pm 0.10$	$8.24 \pm 0.10$	$8.18 \pm 0.10$	–	$8.12 \pm 0.16$

\*H II regions with Wolf-Rayet features.

This paper has been typeset from a  $\text{T}_{\text{E}}\text{X}/\text{L}^{\text{A}}\text{T}_{\text{E}}\text{X}$  file prepared by the author.